https://doi.org/10.5194/egusphere-2026-2893
Preprint. Discussion started: 16 June 2026

Facility-scale quantification and monitoring of ammonia (NH_3) emissions using ASTER multispectral thermal infrared observations

Lidewij B. Tijhuis[1], Tyler Wizenberg[1], and Enrico Dammers[1, 2]

[1]Netherlands Organization for Applied Scientific Research (TNO), Air Quality and Emissions Research (AER), Utrecht, The Netherlands
[2]Institute of Environmental Science (CML), Leiden University, Leiden, The Netherlands

Correspondence: Lidewij B. Tijhuis (lidewij.tijhuis@tno.nl)

Abstract. Ammonia (NH_3) is an important atmospheric pollutant affecting air quality, ecosystems, and climate, but current satellite observations remain limited in their ability to resolve individual emission sources. Hyperspectral thermal infrared sounders such as IASI and CrIS provide broad spatial coverage and high spectral sensitivity, but their kilometer-scale footprints limit direct facility-scale source attribution. Here, we investigate whether high-spatial-resolution multispectral thermal infrared imaging can detect NH_3 plumes at facility scale.

We develop a physically based retrieval framework for the Advanced Spaceborne Thermal Emission and Reflection Radiometer (ASTER), combining radiative transfer calculations with lookup table (LUT) inversion. The method exploits the differential sensitivity of ASTER bands 13 and 14 to NH_3 absorption in the ν_2 band near 930–970 cm^{-1} and retrieves NH_3 column enhancements at 90 m spatial resolution.Surface emissivity is taken from a long-term ASTER emissivity climatology, while scene-level emissivity products are used diagnostically to identify plume-related band behavior. Sensitivity tests show that NH_3 absorption can remain measurable after convolution with the ASTER spectral response functions, but retrieval performance depends strongly on thermal contrast between the surface and the NH_3-bearing layer.

The retrieval is applied to ASTER observations over three industrial NH_3 point sources: Khor Al Zubair, Tolyatti, and Piesteritz. Khor Al Zubair provides the clearest demonstration, with repeated source-connected plume structures under favorable arid conditions. Tolyatti and Piesteritz show that detection is also possible in more heterogeneous environments, although only under suitable thermal contrast and surface conditions. Source-rate estimates derived with the Integrated Mass Enhancement method are interpreted as instantaneous effective estimates for successful plume scenes, not as annual mean emissions or continuous facility-average emissions. Where independent constraints are available, ASTER-derived source-rate statistics are consistent in magnitude with published satellite and airborne estimates.

These results demonstrate that multispectral TIR imagers can provide high-resolution information on NH_3 plume structure and source location, complementing coarse-resolution hyperspectral satellite observations. The approach is best suited for large, persistent sources and episodic plume mapping rather than routine monitoring, because ASTER sampling is limited by revisit frequency, cloud cover, and thermal contrast. The framework supports retrospective analysis of archival ASTER scenes and informs future high-resolution TIR imaging concepts for NH_3 point-source detection.

https://doi.org/10.5194/egusphere-2026-2893
Preprint. Discussion started: 16 June 2026

1 Introduction

Ammonia (NH_3) is a key atmospheric pollutant with significant impacts on air quality, ecosystem health, and climate. It is primarily emitted from agricultural activities, including livestock farming and fertilizer application, as well as from industrial processes and biomass burning (Galloway et al., 2003; Erisman et al., 2008). In the atmosphere, NH_3 reacts with acidic species to form secondary inorganic aerosols, contributing to fine particulate matter ($PM_{2.5}$) and associated health risks (Brunekreef and Holgate, 2002; Fowler et al., 2009). Deposition of reactive nitrogen also contributes to soil acidification and eutrophication, leading to biodiversity loss and ecosystem degradation (Bobbink et al., 1998; De Vries et al., 2015).

Despite its importance, NH_3 remains one of the most poorly constrained atmospheric trace gases. Emission inventories are highly uncertain, with uncertainties often exceeding 50 %, and exhibit strong temporal variability linked to agricultural practices and meteorological conditions (Skjøth and Geels, 2013; Kuenen et al., 2022). Ground-based measurements provide valuable constraints, but their spatial coverage is limited and they are often unable to capture localized emissions and short-term variability.

Satellite observations have substantially improved global monitoring of NH_3 (Van Damme et al., 2014; Shephard et al., 2020). Hyperspectral thermal infrared (TIR) sounders such as the Infrared Atmospheric Sounding Interferometer (IASI) (Hilton et al., 2012) and the Cross-track Infrared Sounder (CrIS) (Han et al., 2013) provide daily global coverage and have revealed numerous previously unidentified NH_3 emission hotspots (Van Damme et al., 2018; Dammers et al., 2019; Clarisse et al., 2023). However, their coarse spatial resolution, typically 14–15 km at nadir, limits their ability to resolve individual sources and small-scale plumes. As a result, only the largest and most isolated sources can be reliably detected, while smaller or clustered emitters often remain unresolved even when long-term averaging is applied (Van Damme et al., 2018).

Recent advances in remote sensing have shown that high-spatial-resolution trace-gas retrievals are possible with multispectral band imagers. Instruments such as Sentinel-2 have been used to detect methane (CH_4) plumes at sub-hundred-meter resolution by exploiting strong absorption features and high signal-to-noise ratios despite limited spectral information (Varon et al., 2019; Cusworth et al., 2022; Gorroño et al., 2023). More recently, multispectral visible-band imagery from Sentinel-2 and Landsat has been used to detect nitrogen dioxide (NO_2) plumes from individual point sources at similar spatial scales (Varon et al., 2024). In the thermal infrared, recent studies indicate that NH_3 detection does not necessarily require full hyperspectral coverage, provided that a limited number of spectral channels sample the strongest absorption features in the ν_2 band (Noppen et al., 2025). Airborne hyperspectral measurements have further demonstrated that NH_3 plumes from individual facilities can be directly observed and quantified at meter-scale resolution (Kuai et al., 2019; Noppen et al., 2023).

In this study, we assess whether NH_3 plumes can be detected using a multispectral TIR satellite imager. We focus on the Advanced Spaceborne Thermal Emission and Reflection Radiometer (ASTER), which provides TIR observations at 90 m spatial resolution in five broad spectral bands. Although ASTER was not designed for atmospheric trace-gas retrievals, it has previously been used to retrieve volcanic SO_2 plumes using TIR band ratios (Campion et al., 2010). Band 13 overlaps with the NH_3 ν_2 absorption region between approximately 930 and 970 cm^{-1} (10.338 μm and 10.753 μm in wavelength). This

https://doi.org/10.5194/egusphere-2026-2893
Preprint. Discussion started: 16 June 2026

spectral overlap suggests that ASTER may retain sensitivity to NH_3 under favorable thermal contrast conditions, despite its broad spectral response functions.

We develop a physically based retrieval framework that combines radiative transfer modeling with a LUT-based inversion. The retrieval uses the differential response of ASTER bands 13 and 14, ASTER GED V3 emissivity information, scene-level radiance correction, plume masking, and IME-based source-rate estimation. Using sensitivity simulations and real ASTER observations, we quantify the dependence of NH_3 detectability on spectral sensitivity, thermal contrast, emissivity, and radiometric noise. We then apply the method to selected industrial point sources to evaluate whether ASTER can resolve facility-scale NH_3 plumes and provide instantaneous source-rate estimates for successful plume scenes.

This work provides a first demonstration that high-resolution multispectral TIR imagery can detect and resolve NH_3 plumes at facility scale. By bridging the gap between coarse-resolution hyperspectral sounders and high-resolution land imagers, the approach offers a complementary pathway for localized atmospheric pollution monitoring, retrospective plume analysis using the ASTER archive, and future missions aiming to combine improved spatial, spectral, and temporal sampling.

2 Methodology and datasets

Figure 1 provides an overview of the full ASTER NH_3 retrieval and emission quantification workflow used in this study. The methodology consists of three main components: radiative transfer modeling and lookup table construction, NH_3 column retrieval from ASTER TIR observations, and plume detection with subsequent emission quantification.

https://doi.org/10.5194/egusphere-2026-2893
Preprint. Discussion started: 16 June 2026

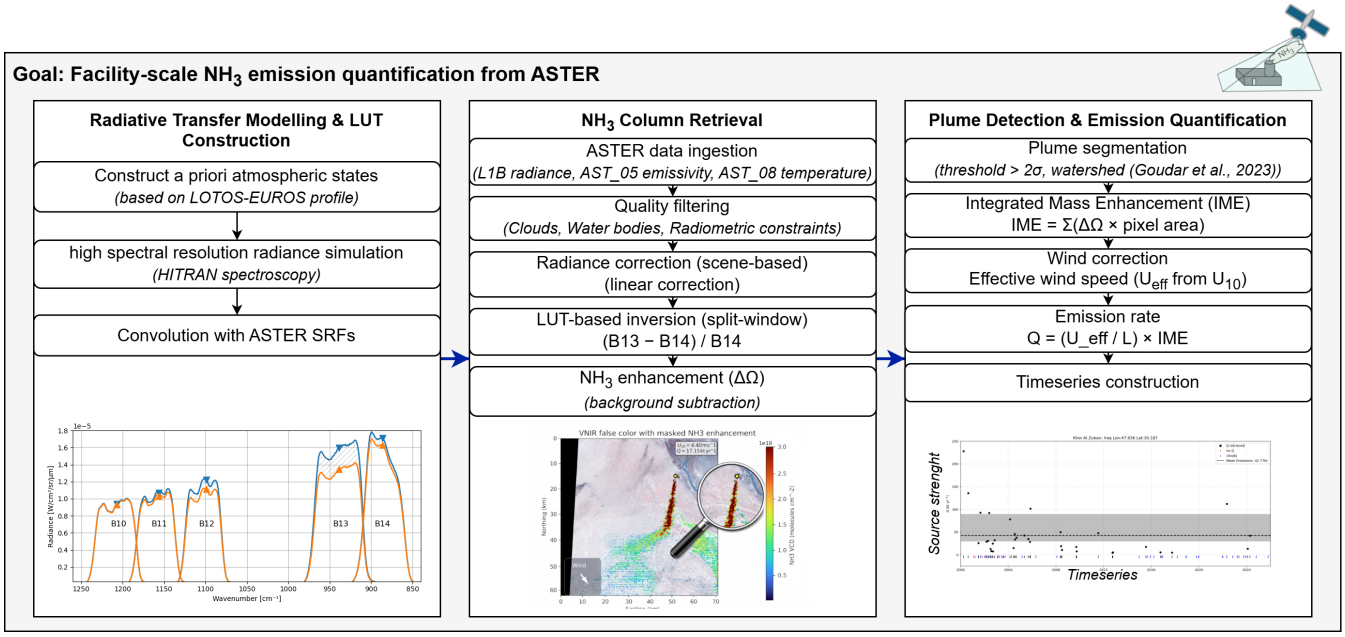

Figure 1. Schematic overview of the ASTER-based NH_3 retrieval and emission quantification workflow. The left panel illustrates radiative transfer modelling and LUT construction using high-resolution simulations convolved with ASTER spectral response functions. The central panel shows ASTER data ingestion, quality filtering, scene-based radiance correction, and LUT-based NH_3 column retrieval using the split-window observable. The right panel summarizes plume detection, Integrated Mass Enhancement (IME) calculation, wind-based emission estimation, and time-series construction.

2.1 ASTER instrument

ASTER is a high-resolution imaging instrument onboard NASA's Terra satellite, providing thermal infrared (TIR) observations at 90 m spatial resolution with a nominal revisit time of approximately 16 days (Yamaguchi et al., 1998; Abrams et al., 2015). The ASTER TIR subsystem operated from March 2000 until January 2026, providing a multi-decadal archive of high-spatial-resolution TIR observations suitable for retrospective plume analysis. In this study, ASTER observations are obtained from the Level 1B radiance product (AST_L1B, Version 4), together with the corresponding surface emissivity product (AST_05, Version 4) and surface kinetic temperature product (AST_08, Version 4) (NASA/METI/AIST/Japan Spacesystems and U.S./Japan ASTER Science Team, 2025a, b, c). The Level 1B product provides calibrated TIR radiances, while AST_05 and AST_08 provide surface properties used for scene characterization and retrieval filtering. Surface emissivity information is also taken from the ASTER Global Emissivity Dataset (GED), which provides multi-year mean emissivities derived from the ASTER archive (NASA JPL, 2014).

The ASTER TIR subsystem comprises five spectral bands, bands 10–14. Ammonia (NH_3) has a strong thermal-infrared absorption feature associated with its ν_2 umbrella-bending vibrational band, located near 930–970 cm^{-1}. Bands 13 and 14 are therefore central to the NH_3 retrieval. Band 13 covers approximately 913–976 cm^{-1} and overlaps with the strongest part of

https://doi.org/10.5194/egusphere-2026-2893
Preprint. Discussion started: 16 June 2026

the NH_3 absorption feature, while band 14 covers approximately 859–913 cm^{-1} and provides a nearby reference channel with weaker NH_3 sensitivity. Band 10 has negligible NH_3 sensitivity but relatively strong H_2O sensitivity, and is therefore useful for diagnostic checks to distinguish NH_3 absorption from water-vapor-related radiance variability.

Under positive thermal contrast, where the surface is warmer than the NH_3-bearing air layer, NH_3 absorption in the ν_2 band reduces the top-of-atmosphere (TOA) radiance measured in band 13. Because band 14 is less sensitive to NH_3, the differential response between bands 13 and 14 forms the basis for the split-window retrieval used in this study. Figure 2 shows the ASTER TIR spectral response functions together with simulated optical depths for relevant atmospheric species.

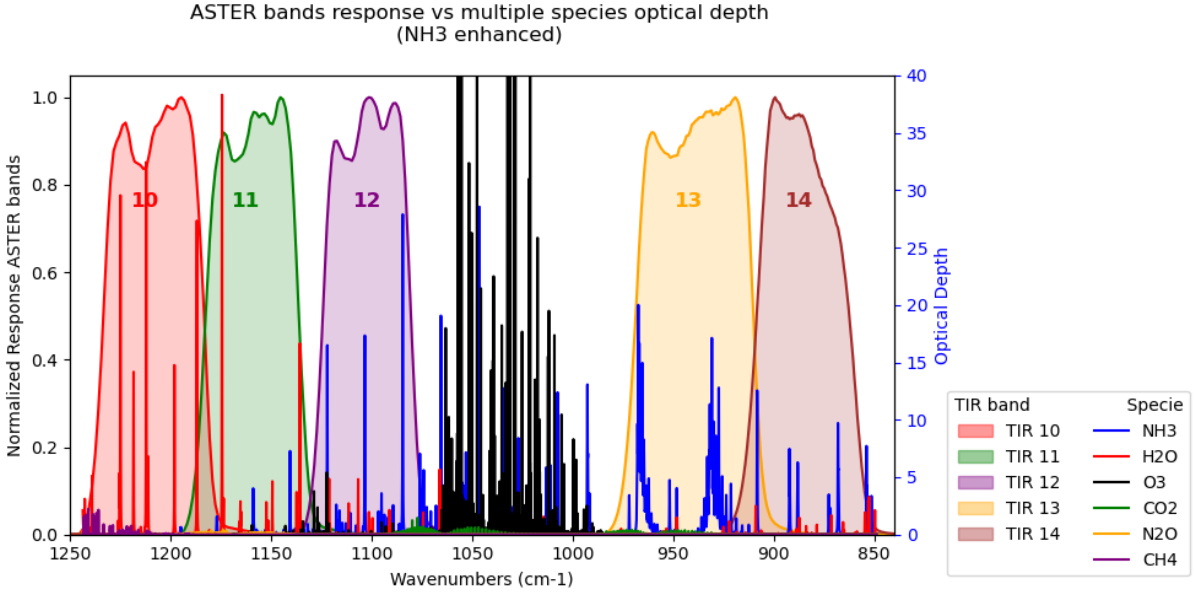

Figure 2. ASTER TIR spectral response functions for bands 10–14 overlaid with simulated optical depth for relevant atmospheric species. Enhanced NH_3 absorption is concentrated in band 13 near 930–970 cm^{-1}, where increased optical depth reduces TOA radiance under positive thermal contrast conditions. Band 14 provides a nearby reference with weaker NH_3 sensitivity, forming the basis for the split-window retrieval approach.

The detectability of NH_3 is constrained not only by spectral overlap, but also by the radiometric performance of the ASTER TIR instrument. ASTER has demonstrated stable radiometric behavior supported by onboard and vicarious calibration (Abrams et al., 2015). The noise-equivalent temperature difference (NEΔT) is approximately 0.3 K at 300 K, with typical scene-based noise levels of about 0.1–0.2 K (Arai and Tonooka, 2005). Under favorable thermal contrast, NH_3-induced radiance differences can exceed these noise levels, enabling detection in individual scenes.

ASTER TIR observations can exhibit weak horizontal striping associated with detector-to-detector calibration differences. This can introduce band-correlated background variability in emissivity and radiance fields (Gillespie et al., 2011). These patterns are generally small compared with NH_3 plume signals under favorable thermal contrast. Their impact is reduced by

https://doi.org/10.5194/egusphere-2026-2893
Preprint. Discussion started: 16 June 2026

scene-level radiance correction and the use of band ratios. Residual striping may nevertheless contribute to low-amplitude background variability in some scenes.

2.2 Radiative transfer framework

Radiative transfer in the thermal infrared determines the top-of-atmosphere (TOA) radiance measured by ASTER through the combined effects of surface emission, atmospheric absorption, and atmospheric emission. In this study, NH_3 column densities are retrieved using a physically based forward-modeling approach in which simulated ASTER band radiances are compared with observed radiances.

Radiative transfer calculations are performed with TFIT, a Python-based radiative transfer model developed at TNO. TFIT uses spectroscopic parameters from the HITRAN database through the HAPI interface (Kochanov et al., 2016) and explicitly represents gas absorption, surface emissivity, and atmospheric temperature profiles on a flexible vertical grid. High-resolution spectral radiances are calculated and subsequently convolved with the ASTER spectral response functions (SRFs) to obtain band-integrated radiances consistent with the ASTER observations.

To enable efficient retrievals, TFIT simulations are stored in a multidimensional lookup table (LUT; Sect. 2.3.1). The LUT spans NH_3 column amount, surface emissivity, near-surface air temperature, and surface temperature. This avoids repeated radiative transfer calculations during scene processing while preserving a physically consistent mapping between atmospheric state and observed radiance.

Figure 3 illustrates the effect of NH_3 on TOA radiance for two otherwise identical simulations. A background-like case with an NH_3 column of 10^{15} molecules cm^{-2} is compared with a strong plume enhancement of 10^{19} molecules cm^{-2}. The elevated NH_3 case shows localized radiance reductions relative to the low-NH_3 case, most prominently in the 930–970 cm^{-1} region corresponding to the NH_3 ν_2 band. These perturbations remain visible after convolution with the ASTER SRFs, as shown in Fig. 3c, producing measurable differences in band-integrated radiances.

The radiative transfer modelling and LUT construction steps are summarized schematically in the left panel of Fig. 1.

https://doi.org/10.5194/egusphere-2026-2893
Preprint. Discussion started: 16 June 2026

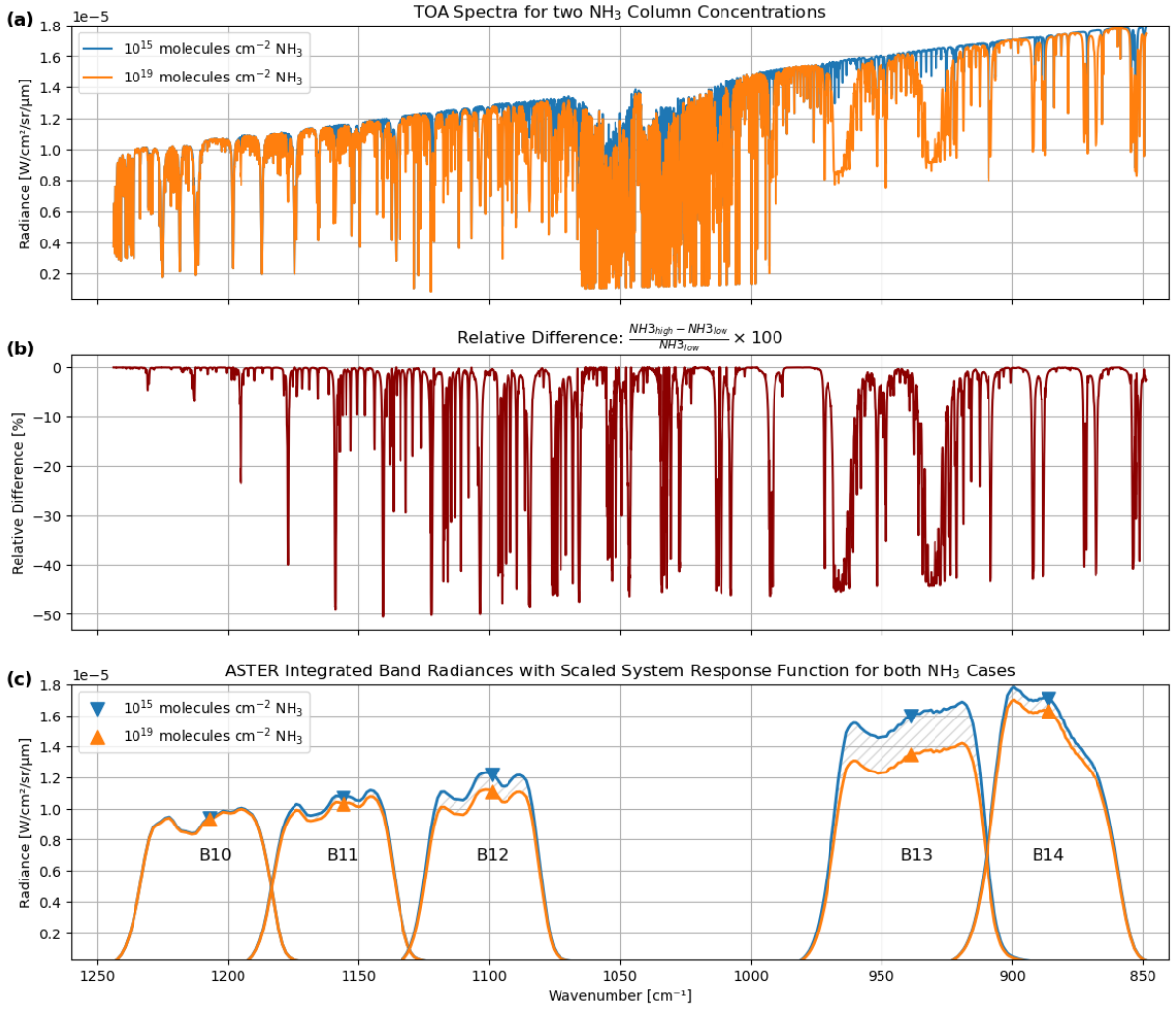

Figure 3. (a) Simulated high-resolution TOA radiance spectra for two NH_3 column amounts (10^{15} and 10^{19} molecules cm^{-2}), illustrating absorption features across 880–1220 cm^{-1}. (b) Relative radiance difference between the two cases, highlighting the narrow spectral structure of NH_3 absorption in the ν_2 band. (c) ASTER spectral response functions for bands 10–14, shaded curves, overlaid with corresponding band-integrated radiances for both NH_3 cases, illustrating how high-resolution NH_3 absorption features map into broadband ASTER measurements.

2.3 Retrieval strategy

The retrieval steps outlined in the central panel of Fig. 1 are described in detail below.

Building on the ASTER band characteristics described in Sect. 2.1 and the LUT-based radiative transfer simulations described in Sect. 2.2, the retrieval strategy exploits the differential sensitivity of ASTER bands 13 and 14 to NH_3 absorption to derive column enhancements from a split-window observable.

https://doi.org/10.5194/egusphere-2026-2893
Preprint. Discussion started: 16 June 2026

ASTER provides only five broad TIR bands and therefore cannot resolve individual NH_3 absorption lines in the same way as hyperspectral sounders such as IASI and CrIS. The retrieval strategy used here instead relies on the differential response of ASTER bands 13 and 14. The operational retrieval therefore uses the split-window observable

$$R = \frac{L_{13} - L_{14}}{L_{14}}, \tag{1}$$

where L_{13} and L_{14} are the ASTER TOA radiances in bands 13 and 14, respectively.

This observable enhances the differential NH_3 signal while reducing sensitivity to scene-wide thermal variability that affects both bands. Because the NH_3 signal remains small compared with the total TIR radiance, the retrieval depends critically on accurate treatment of surface temperature, surface emissivity, thermal contrast, and radiometric noise. The method therefore combines a LUT-based forward model, scene-level radiance correction, plume detection, and IME-based flux estimation.

2.3.1 Lookup table construction

To avoid full radiative transfer calculations for every pixel, a multidimensional LUT of TFIT-simulated radiances is constructed. The LUT spans NH_3 column amount, surface emissivity, near-surface air temperature, and surface temperature (Table 1). These parameters represent the dominant controls on the ASTER NH_3 signal. For scene application, the emissivity dimension is constrained using ASTER GED V3 emissivity values mapped to the ASTER TIR grid, so that the LUT inversion uses a climatological emissivity input rather than the potentially plume-affected scene emissivity retrieval.

For each LUT state, TFIT calculates high-resolution spectral radiances that are convolved with the ASTER SRFs to obtain band-integrated radiances. NH_3 is prescribed in the lowest 500 m of the atmosphere, reflecting the near-surface character of most industrial plumes. The prescribed column amount is converted to layer mixing ratios using temperature-dependent air density and layer thickness. The lowest model level, at approximately 60 m, is set to the prescribed air temperature T_{air}, while the profile above is adjusted smoothly to preserve a realistic vertical structure.

Surface temperature is varied relative to T_{air} to sample a wide range of thermal contrast conditions:

$$TC = T_{\mathrm{surface}} - T_{\mathrm{air}}. \tag{2}$$

Because NH_3 is distributed over the lowest 500 m, this definition should be interpreted as a near-surface thermal contrast rather than the exact layer-mean contrast experienced by the gas. This distinction becomes important near $TC = 0$ K, where retrieval sensitivity collapses and can change sign.

https://doi.org/10.5194/egusphere-2026-2893
Preprint. Discussion started: 16 June 2026

Table 1. Parameter space used to construct the NH_3 LUT.

Parameter	Range / values	Description
NH_3 column	10^{15}–10^{20} molecules cm^{-2}	Applied in the lowest 500 m and converted to layer mixing ratios using temperature-dependent air density.
Surface emissivity	0.80–1.00	Discrete emissivity values combined with each atmospheric case.
Air temperature T_{air}	270–340 K	Prescribed temperature at the lowest model level, approximately 60 m. The profile above is adjusted smoothly.
Surface temperature T_{surface}	$T_{\mathrm{air}} - 10$ K to $T_{\mathrm{air}} + \Delta_{\mathrm{warm}}$	Δ_{warm} is +30 K for $T_{\mathrm{air}} < 290$ K, +40 K for $290 \leq T_{\mathrm{air}} < 310$ K, and +50 K for $T_{\mathrm{air}} \geq 310$ K.
Thermal contrast	$TC = T_{\mathrm{surface}} - T_{\mathrm{air}}$	Difference between surface temperature and the lowest atmospheric model level.

2.3.2 Scene-based radiance correction

Before inversion, a scene-based radiance correction is applied to reduce systematic offsets between the observed ASTER Level 1B radiances and the LUT-simulated radiances. These offsets can arise from residual calibration differences, imperfect representation of surface emissivity, uncertainties in the atmospheric temperature profile, and simplifications in the forward model. Because the NH_3 signal in ASTER's broad TIR bands is small compared with the total scene radiance, such offsets must be minimized before calculating the NH_3-sensitive band ratio.

The correction is derived independently for each TIR band using a reduced major axis (RMA) regression between observed and LUT-simulated radiances. RMA regression is used because both the observed and simulated radiances contain uncertainty, and the correction is intended to align the radiometric background rather than to treat one quantity as error-free. The fit is performed over pixels that pass the scene quality selection and have finite, non-zero observed and simulated radiances in the NH_3-sensitive bands.

To reduce the influence of outliers, the regression is fitted after percentile filtering. For each band, observed and simulated radiances are first extracted over the valid scene pixels. Pixels outside the 10th–90th percentile range of either the observed or simulated radiance distribution are excluded from the fit. If too few pixels remain after this filtering, the regression is instead fitted using the unfiltered valid pixels. This procedure reduces the influence of clouds, artifacts, strong local surface anomalies, and possible plume pixels on the scene-level correction.

For each band b, the fitted RMA relationship is applied to the observed radiance field as

$$L_b^{\mathrm{corr}} = a_b L_b^{\mathrm{obs}} + c_b, \tag{3}$$

where L_b^{obs} is the observed ASTER radiance, L_b^{corr} is the corrected radiance, and a_b and c_b are the scene-specific RMA slope and intercept. The same correction is applied to all valid pixels in the scene for that band. The correction therefore removes broad scene-level radiometric offsets while preserving local radiance perturbations, including plume-scale structures.

https://doi.org/10.5194/egusphere-2026-2893
Preprint. Discussion started: 16 June 2026

After correction, the NH_3-sensitive split-window observable is calculated from bands 13 and 14 as

$$R^{\mathrm{obs}} = \frac{L_{13}^{\mathrm{corr}} - L_{14}^{\mathrm{corr}}}{L_{14}^{\mathrm{corr}}}. \tag{4}$$

The purpose of the correction is not to remove the plume signal, but to align the observed radiometric background with the LUT-simulated background so that local deviations in the band 13–14 ratio can be interpreted more directly as NH_3 absorption.

For each valid pixel, the NH_3 column is retrieved by comparing the corrected observed ratio with the LUT-simulated ratio. The retrieved column $\hat{\Omega}_{\mathrm{NH_3}}$ is defined as the LUT state that minimizes the squared difference between observation and simulation:

$$\hat{\Omega}_{\mathrm{NH_3}} = \arg\min_{\Omega_{\mathrm{NH_3}}} \left[R^{\mathrm{obs}} - R^{\mathrm{LUT}}\left(\Omega_{\mathrm{NH_3}}, T_{\mathrm{air}}, T_{\mathrm{surface}}, \epsilon\right)\right]^2. \tag{5}$$

Here, T_{air} is the near-surface air temperature, T_{surface} is the ASTER surface temperature, and ϵ is the emissivity. The retrieved NH_3 field is subsequently converted to an enhancement field by subtracting a scene-dependent background before plume detection and flux estimation.

A limitation of this approach is that broad plume enhancements or spatially extensive surface artifacts may partly influence the scene-level correction if they are not removed by the quality and percentile filters. The radiance correction is therefore interpreted as a pragmatic scene-level bias correction, not as an absolute calibration of the ASTER radiances.

2.3.3 Plume detection

Plume detection and emission quantification follow the workflow shown in the right panel of Fig. 1.

Retrieved NH_3 columns are converted to plume enhancements by subtracting a scene-dependent background. The background is estimated from quality-filtered clear-sky pixels outside the immediate source region and is assumed to represent the large-scale atmospheric NH_3 field.

Pixels are used for plume detection only if they satisfy thermal and radiometric quality criteria, have finite retrieval values, and are located within 15 km of the target source. This distance threshold defines the source-centered plume search domain used for the IME calculation. Candidate plume pixels are additionally filtered using a relative retrieval-uncertainty threshold of 60 %, so that pixels with poorly constrained NH_3 columns do not dominate the plume mask or source-rate estimate.

Within this source-centered domain, candidate plume pixels are identified from the background-corrected NH_3 enhancement field. The filtered enhancement field is segmented using a marker-based watershed method following Goudar et al. (2023). So that only plume regions connected to the source location are used for inversion. This approach allows irregular plume shapes while reducing the risk that unrelated background structures are included in the source plume.

The resulting plume mask is used to calculate the Integrated Mass Enhancement (Frankenberg et al., 2016; Varon et al., 2018). Because the 15 km domain limits the spatial extent over which plume mass is integrated, the derived source rates should be interpreted as effective emissions over the observed plume extent rather than as total emissions under all transport conditions.

https://doi.org/10.5194/egusphere-2026-2893
Preprint. Discussion started: 16 June 2026

2.3.4 Integrated Mass Enhancement method

Emission fluxes are estimated using the Integrated Mass Enhancement (IME) method (Frankenberg et al., 2016; Varon et al., 2018). The IME is the total excess NH_3 mass contained within the detected plume:

$$\mathrm{IME} = \sum_j \Delta\Omega_j A_j M_{\mathrm{NH_3}}, \tag{6}$$

where $\Delta\Omega_j$ is the background-corrected NH_3 column enhancement in pixel j, A_j is the pixel area, and $M_{\mathrm{NH_3}}$ converts molecules to mass.

The emission rate is calculated as

$$Q = \frac{U_{\mathrm{eff}}}{L}\mathrm{IME}, \tag{7}$$

where L is a characteristic plume length scale and U_{eff} is the effective wind speed. As a first-order approximation, U_{eff} is parameterized from the 10 m wind speed U_{10} following Varon et al. (2018):

$$U_{\mathrm{eff}} = 0.9\ln(U_{10}) + 0.6. \tag{8}$$

This parameterization was originally derived for methane plumes and is not expected to be universally applicable to NH_3. Differences in plume rise, emission height, deposition, chemistry, boundary-layer structure, and source geometry may affect the relationship between U_{10} and U_{eff}. In addition, ERA5 winds represent grid-scale meteorological conditions and may not capture plume-scale flow at the source, the plume height, or the exact ASTER overpass time. Wind speed and wind direction should therefore be interpreted as transport constraints for the IME calculation rather than as exact descriptions of the observed plume motion.

The main uncertainty terms in Q arise from radiometric noise in the retrieved column, background subtraction, plume masking, wind speed, wind direction, wind-field representativeness, the U_{eff} parameterization, surface emissivity assumptions, and the vertical distribution of NH_3. Potential absorption by co-emitted or ambient species within the ASTER bands can also bias the retrieved NH_3 column because the current LUT treats NH_3 as the only variable absorber.

2.4 Target locations

Three target locations were selected to span a range of source strengths and observing conditions: Khor Al Zubair in Iraq, Tolyatti in Russia, and Piesteritz in Germany. Candidate sites were selected from known industrial NH_3 point sources identified in satellite-based hotspot studies (Dammers et al., 2019; Van Damme et al., 2018). The selection criteria were persistent and well-documented NH_3 emissions, availability of ASTER observations, and suitability for testing the retrieval under different surface and thermal conditions. Piesteritz was included specifically because independent airborne hyperspectral thermal infrared observations are available for this site (Noppen et al., 2023), providing an external reference for evaluating ASTER performance near the practical detection limit.

https://doi.org/10.5194/egusphere-2026-2893
Preprint. Discussion started: 16 June 2026

Khor Al Zubair (47.836° E, 30.187° N) is used as the benchmark case. The source is located in a hot arid environment with frequent positive thermal contrast and generally limited cloud contamination, making it well suited for demonstrating the full retrieval chain.

Tolyatti (49.614° E, 53.544° N) is one of the largest known industrial NH_3 point sources, but is located in a more heterogeneous temperate environment. The site therefore provides a test of ASTER performance under less favorable surface and thermal conditions.

Piesteritz (12.586° E, 51.876° N) represents a smaller but well-characterized European industrial source and is used here to evaluate ASTER performance close to the practical detection limit.

Table 2 summarizes the number of ASTER scenes processed and the number of scenes with successful NH_3 plume detections for each target location.

Table 2. Summary of ASTER scene availability and retrieval success for the three target locations. Scenes processed denotes the total number of ASTER scenes. Successful detections denotes scenes with a detected NH_3 emission.

Site	Scenes processed	Not cloudy	Successful detections
Khor Al Zubair	75	41	33
Tolyatti	67	12	10
Piesteritz	136	27	6

3 Results

3.1 Sensitivity analysis

The detectability of NH_3 in ASTER TIR observations depends on three coupled factors: the spectral sensitivity of the bands, thermal contrast between the surface and the NH_3-bearing layer, and radiometric noise. In this section, these dependencies are quantified using forward-modeled ASTER band-integrated radiances, as well as band differences and ratios involving bands 13 and 14. Following the logic of Campion et al. (2010), emphasis is placed on band differences and ratios that enhance the NH_3 signal while reducing sensitivity to scene-wide thermal variability and spectral interference from other absorbers.

3.1.1 Spectral sensitivity and band selection

Figure 4 shows the simulated response of ASTER bands 10–14 to increasing NH_3 column amount for a fixed atmospheric temperature of 300 K, surface temperature of 320 K, and thermal contrast of 20 K. Band 13 (yellow diamonds) is already sensitive at lower NH_3 columns, showing a clear radiance decrease consistent with its overlap with the NH_3 ν_2 absorption band. Band 14 (orange triangles) shows a weaker response and is therefore suitable as a nearby reference channel.

Band 12 (blue triangles) also shows a pronounced radiance decrease, but the slope of its response increases mainly at higher NH_3 column densities. This favors band 13 for its lower sensitivity threshold. In addition, band 12 lies in a more spectrally

https://doi.org/10.5194/egusphere-2026-2893
Preprint. Discussion started: 16 June 2026

crowded region where the ASTER response overlaps with absorption from other atmospheric species (Fig. 2). This makes band 12 more susceptible to interference from co-emitted or variable background species, and therefore less suitable as the primary retrieval channel. Bands 10 and 11 are not used for the primary NH_3 inversion, but provide diagnostic information on scene consistency and possible contamination by other absorbers.

The split-window observable $(B13 - B14)/B14$ is selected because it combines strong NH_3 sensitivity in band 13 with the weaker, spectrally adjacent response of band 14. This ratio preserves the differential NH_3 signal while reducing common thermal background variability between neighboring bands.

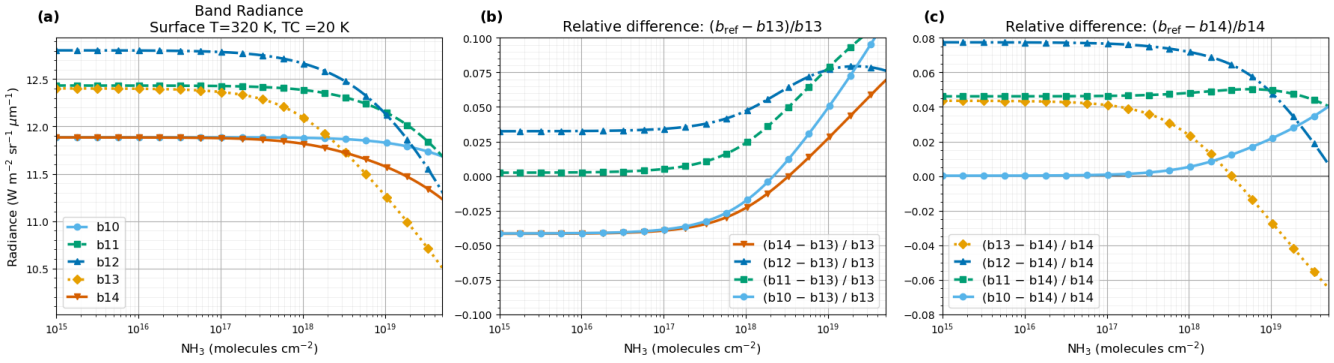

Figure 4. Sensitivity of ASTER TIR bands to NH_3 for a surface temperature of 320 K and a thermal contrast of 20 K. (a) Absolute radiances for bands 10–14 as a function of NH_3 column amount. Band 13 shows a clear radiance depression already at lower NH_3 columns, consistent with overlap with the NH_3 ν_2 absorption band. Band 12 also responds strongly, but its steep radiance decrease occurs mainly at higher NH_3 columns. (b) Relative differences $(b_{\mathrm{ref}} - b13)/b13$, showing that band contrasts involving band 13 preserve a monotonic NH_3 dependence. (c) Relative differences $(b_{\mathrm{ref}} - b14)/b14$, where $(b13 - b14)/b14$ provides the primary NH_3-sensitive split-window observable used in the retrieval.

3.1.2 Role of thermal contrast in NH_3 detectability

Thermal contrast controls both the magnitude and the sign of the NH_3 signal in the TIR. This is a general limitation of ASTER TIR trace-gas retrievals, as also shown for SO_2 by Campion et al. (2010). To investigate this dependence, surface temperature was varied between 306 and 336 K while the near-surface air temperature was fixed at 300 K. Figure 5 shows the resulting band 13 radiance and split-window ratio for these thermal contrast conditions.

For positive thermal contrast ($T_{\mathrm{sfc}} > T_{\mathrm{air}}$), NH_3 absorbs radiation from the warmer surface background, reducing the top-of-atmosphere radiance measured in band 13. A larger temperature difference between the surface and the NH_3-bearing layer increases this absorption contrast, steepening the split-window response. Retrieval sensitivity therefore improves as positive thermal contrast increases.

When surface and atmospheric temperatures are similar, the NH_3 signal collapses and retrievals become noise dominated. For negative thermal contrast, where $T_{\mathrm{sfc}} < T_{\mathrm{air}}$, the signal can reverse sign because emission from the warmer NH_3-bearing

https://doi.org/10.5194/egusphere-2026-2893
Preprint. Discussion started: 16 June 2026

layer can exceed the colder surface contribution. This regime is physically meaningful, but as a strong enough negative thermal contrast rarely occurs, it is not the target regime for this study.

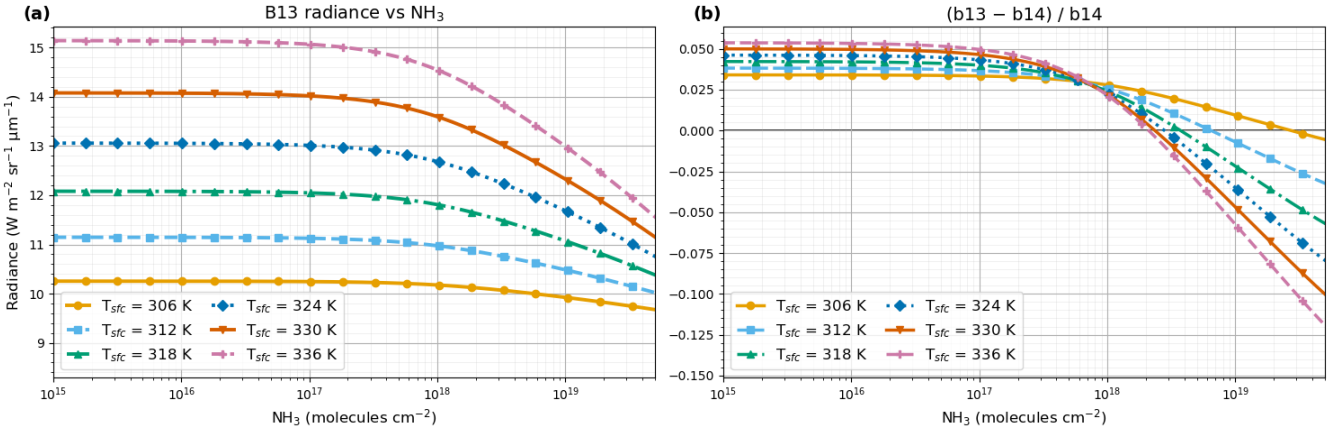

Figure 5. Dependence of the ASTER NH_3 signal on surface temperature and thermal contrast. (a) Band 13 radiance as a function of NH_3 column amount for surface temperatures between 306 and 336 K, with the near-surface air temperature fixed at 300 K. (b) Corresponding split-window ratio $(B13 - B14)/B14$. Increasing surface temperature, and therefore increasing positive thermal contrast, strengthens the NH_3 absorption signal in band 13 and steepens the ratio response. At low thermal contrast the radiance and ratio vary only weakly with NH_3, whereas at high thermal contrast the separation between NH_3 columns increases strongly.

3.1.3 Joint sensitivity to NH_3 and thermal contrast

The two-dimensional sensitivity of the split-window observable is shown in Fig. 6 as a function of NH_3 column amount and thermal contrast. The figure shows that ASTER detectability is not controlled by NH_3 column alone, but by the combined state of column amount and thermal contrast.

Near zero thermal contrast, the ratio remains nearly flat across all NH_3 columns because radiance sensitivity approaches zero. As thermal contrast increases, the ratio develops a progressively stronger dependence on NH_3, becoming more negative at high NH_3 burden as band 13 absorption strengthens relative to band 14. The most favorable retrieval regime occurs when both NH_3 loading and positive thermal contrast are high.

https://doi.org/10.5194/egusphere-2026-2893
Preprint. Discussion started: 16 June 2026

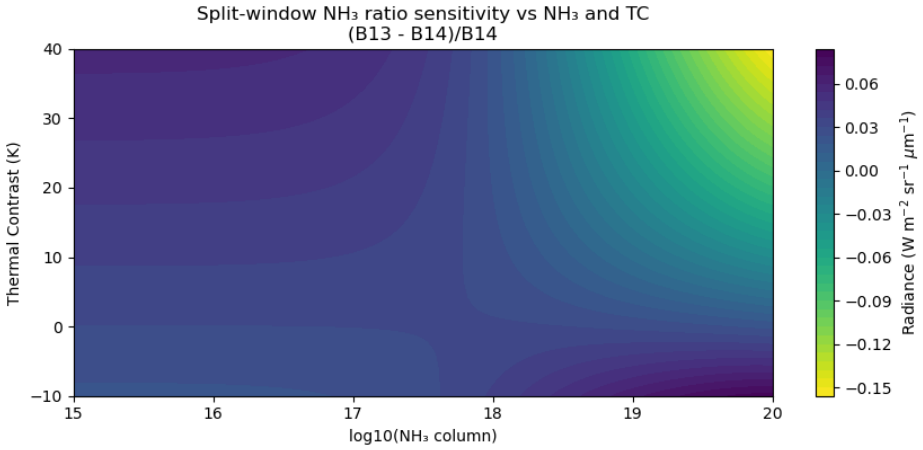

Figure 6. Two-dimensional sensitivity of the split-window observable $(B13-B14)/B14$ to NH_3 column amount and thermal contrast for a lower-atmospheric temperature of 300 K. Contours show the LUT-simulated ratio for combinations of NH_3 and $T_{\mathrm{sfc}}-T_{\mathrm{air}}$. For low thermal contrast, the ratio varies only weakly with NH_3. As thermal contrast increases, the ratio becomes strongly sensitive to NH_3. Negative thermal contrast produces a sign reversal consistent with emission-like behavior.

3.1.4 Radiometric noise and uncertainty propagation

Radiometric noise sets the lower limit of detectable NH_3 enhancement and propagates directly into retrieval uncertainty. ASTER TIR noise is expressed as a noise-equivalent temperature difference (NEΔT), which is converted to radiance noise using the Planck function. The resulting radiance noise is then propagated through the LUT-derived sensitivities. This follows the noise-equivalent gas-column approach used by Campion et al. (2010), adapted here to NH_3 and to the band 13–14 split-window ratio.

For a single band, the noise-equivalent NH_3 column is

$$\mathrm{NE}\Delta\Omega_{\mathrm{NH_3}} = \frac{\sigma_L}{|\partial L/\partial\Omega_{\mathrm{NH_3}}|}, \tag{9}$$

where σ_L is the radiance noise and $\partial L/\partial\Omega_{\mathrm{NH_3}}$ is evaluated from the LUT. This quantity represents the column enhancement that would produce a radiance perturbation comparable to the instrumental noise.

For the split-window ratio, the radiance noise from bands 13 and 14 is propagated as

$$\sigma_R^2 = \left(\frac{\partial R}{\partial L_{13}}\right)^2 \sigma_{L,13}^2 + \left(\frac{\partial R}{\partial L_{14}}\right)^2 \sigma_{L,14}^2, \tag{10}$$

where

$$\frac{\partial R}{\partial L_{13}} = \frac{1}{L_{14}}, \qquad \frac{\partial R}{\partial L_{14}} = -\frac{L_{13}}{L_{14}^2}. \tag{11}$$

The corresponding NH_3 uncertainty is obtained by dividing the ratio uncertainty by the local LUT sensitivity:

$$\sigma_{\mathrm{NH_3}} = \frac{\sigma_R}{|\partial R/\partial\Omega_{\mathrm{NH_3}}|_{\mathrm{ret}}}. \tag{12}$$

https://doi.org/10.5194/egusphere-2026-2893
Preprint. Discussion started: 16 June 2026

Figure 7 shows the resulting noise-equivalent NH_3 column as a function of thermal contrast. Around zero thermal contrast, the LUT sensitivity to NH_3 becomes weak and the noise-equivalent column increases sharply. For stronger thermal contrast, the LUT sensitivity steepens and the noise-equivalent column decreases to values of order 10^{17}–10^{18} molecules cm^{-2}.

These values should be interpreted as theoretical single-pixel sensitivity limits. In real ASTER scenes, robust plume detection is more restrictive because the retrieval also depends on spatial coherence, surface heterogeneity, background subtraction, plume masking, residual radiance artifacts, and possible spectral interference. The limits shown in Fig. 7 therefore represent lower-bound sensitivity estimates rather than guaranteed plume detection thresholds.

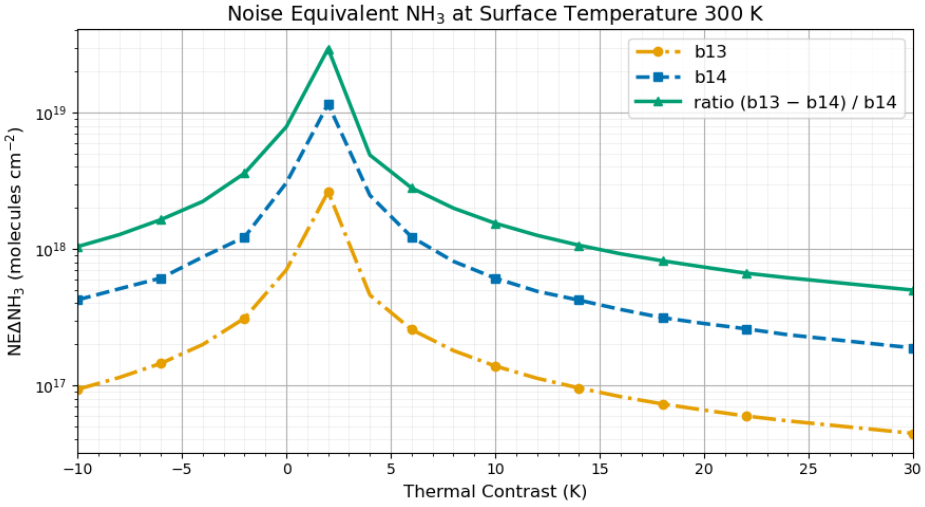

Figure 7. Noise-equivalent NH_3 column as a function of thermal contrast for ASTER bands 13 and 14 and the split-window ratio $(B13 - B14)/B14$, derived from LUT-based TOA radiance sensitivities at a fixed surface temperature of 300 K. Around zero thermal contrast the NH_3 sensitivity is weak, while stronger thermal contrast reduces the noise-equivalent column to values of order 10^{17}–10^{18} molecules cm^{-2}.

3.2 Demonstration of the retrieval workflow

The ASTER retrieval workflow consists of five main steps. First, ASTER TIR radiances, VNIR imagery, surface temperature, emissivity information, and quality flags are ingested and mapped to the TIR grid. Pixels affected by clouds, artifacts, invalid radiances, or unrealistic surface temperatures are removed using product quality flags and scene-level filters.

Second, surface emissivity is taken from the ASTER Global Emissivity Database Version 3 (ASTER GED V3). This product provides multi-year mean land-surface emissivities derived from the ASTER archive and is used here as the emissivity input for the LUT retrieval. Using a climatological emissivity product reduces the risk that plume-induced radiance reductions in an individual ASTER scene are incorrectly interpreted as scene-specific emissivity depressions. The emissivity information is nevertheless an important source of uncertainty. Spatial variations in mineral composition, land cover, dust, and surface structure can introduce band-dependent radiance variability that is not caused by NH_3 (Ginoux et al., 2012; Someya et al.,

https://doi.org/10.5194/egusphere-2026-2893
Preprint. Discussion started: 16 June 2026

2020). Dust also has a distinct thermal-infrared spectral signature and can introduce surface-emissivity-related biases over desert surfaces, making dust-prone scenes particularly challenging for weak trace-gas retrievals (Clarisse et al., 2019).

The ASTER scene emissivity products are used as diagnostic information. Because scene-level emissivity retrievals assume a standard atmospheric state, unmodeled gas absorption can appear as an apparent emissivity anomaly in the affected band. A plume-shaped depression in band 13 that is absent or weaker in band 14 is therefore consistent with NH_3 absorption and provides an additional visual check. However, the quantitative NH_3 retrieval is based on the GED-derived emissivity input rather than on plume-affected scene emissivity values.

Third, near-surface air temperature from meteorological reanalysis is combined with ASTER surface temperature to estimate the thermal contrast field. Observed ASTER radiances are then corrected using the scene-based RMA correction described in Sect. 2.3.2. The corrected band 13 and band 14 radiances are used to calculate the split-window observable, and each valid pixel is inverted against the LUT to retrieve the NH_3 column.

Fourth, radiometric noise is propagated to a pixel-level NH_3 uncertainty by converting ASTER NEΔT to radiance noise, propagating this noise through the split-window ratio, and dividing by the local LUT-derived sensitivity. Finally, the retrieved NH_3 field is background-corrected, segmented into a plume mask within a 15 km source-centered domain, and integrated to obtain the IME. Combining the IME with wind information provides an instantaneous source-rate estimate.

The following subsections show the resulting retrievals for the three target sites. These examples illustrate both the strengths and limitations of the approach: coherent source-connected plumes can be detected under favorable conditions, while structured background variability, emissivity effects, dust, cloud contamination, and weak thermal contrast can limit retrieval robustness.

Table 3 summarizes the ASTER successful-scene source-rate statistics together with published NH_3 source-rate estimates for the three target sites. The comparison is intended as method-dependent context rather than direct validation. The Van Damme et al. (2018) values are based on nine-year IASI oversampled averages and box-model flux calculations with an assumed NH_3 lifetime of 12 h. The Dammers et al. (2019) values are constrained wind-rotation EMG estimates using fixed lifetime $\tau = 2.5$ h and plume width $\sigma = 15$ km. The Noppen et al. (2023) values are airborne Hyper-Cam LW estimates over Piesteritz derived with IME and cross-sectional flux methods under different plume-rise assumptions. In contrast, the ASTER values reported here are successful-scene instantaneous IME estimates and should not be interpreted as annual mean emissions.

https://doi.org/10.5194/egusphere-2026-2893
Preprint. Discussion started: 16 June 2026

Table 3. Comparison of ASTER successful-scene source-rate statistics with published NH_3 source-rate estimates and inventory values for the three target sites. ASTER values represent instantaneous successful-scene IME estimates from this study and should not be interpreted as annual mean emissions. Literature and inventory values are included as method-dependent context rather than direct validation of individual ASTER overpasses. Van Damme et al. values are based on nine-year IASI oversampled averages and box-model flux calculations with an assumed NH_3 lifetime of 12 h. Dammers et al. values are constrained wind-rotation EMG estimates from CrIS and IASI using fixed lifetime $\tau = 2.5$ h and plume width $\sigma = 15$ km. HTAPv2 values are gridded inventory values from the $1.0^\circ \times 1.0^\circ$ product. Noppen et al. values are airborne Hyper-Cam LW estimates over Piesteritz derived with IME and cross-sectional flux methods under different plume-rise assumptions. The E-PRTR value for Piesteritz is a reported facility-level inventory value from European industrial emissions reporting and is included as inventory context only (European Environment Agency, 2021)

Site	Data source	Study	Method	Source rate
Khor Al Zubair	ASTER	This study	Successful-scene IME mean	~ 52 kt yr^{-1}
Khor Al Zubair	IASI	Van Damme et al. (2018)	Box model, $\tau = 12$ h	3.9 kt yr^{-1}
Khor Al Zubair	CrIS	Dammers et al. (2019)	EMG, $\tau = 2.5$ h, $\sigma = 15$ km	55 kt yr^{-1}
Khor Al Zubair	IASI	Dammers et al. (2019)	EMG, $\tau = 2.5$ h, $\sigma = 15$ km	18–19 kt yr^{-1}
Khor Al Zubair	HTAPv2	Janssens-Maenhout et al. (2015)	$1.0^\circ \times 1.0^\circ$ inventory grid	4.9 kt yr^{-1}
Tolyatti	ASTER	This study	Successful-scene IME mean	~ 31 kt yr^{-1}
Tolyatti	IASI	Van Damme et al. (2018)	Box model, $\tau = 12$ h	7.4 kt yr^{-1}
Tolyatti	CrIS	Dammers et al. (2019)	EMG, $\tau = 2.5$ h, $\sigma = 15$ km	77 kt yr^{-1}
Tolyatti	IASI	Dammers et al. (2019)	EMG, $\tau = 2.5$ h, $\sigma = 15$ km	66–79 kt yr^{-1}
Tolyatti	HTAPv2	Janssens-Maenhout et al. (2015)	$1.0^\circ \times 1.0^\circ$ inventory grid	2.0 kt yr^{-1}
Piesteritz	ASTER	This study	Successful-scene IME mean	~ 4.0 kt yr^{-1}
Piesteritz	Hyper-Cam LW	Noppen et al. (2023)	IME, spring 2021	1.6–3.2 kt yr^{-1}
Piesteritz	Hyper-Cam LW	Noppen et al. (2023)	CSF, spring 2021	2.2–5.4 kt yr^{-1}
Piesteritz	E-PRTR	European Environment Agency (2021)	Reported inventory	0.4 kt yr^{-1}

3.2.1 Khor Al Zubair

Khor Al Zubair provides the most favorable test case for the ASTER NH_3 retrieval. The source is located in a hot arid environment with frequent positive thermal contrast and generally limited cloud contamination. These conditions increase the band 13 radiance depression for a given NH_3 column and make the site well suited for TIR plume detection. However, the arid background is not radiometrically uniform in all scenes. Spatial variability in mineral emissivity, surface temperature, suspended dust, or dust-storm-related TIR radiance can introduce structured retrieval noise and plume-like artifacts away from the source.

Figure 8 shows a successful ASTER retrieval over Khor Al Zubair on 4 April 2000. The retrieved NH_3 enhancement is spatially connected to the source and forms a narrow, coherent plume-like structure. The scene demonstrates the main elements of the retrieval workflow: an NH_3 enhancement in the source region, elevated sensitivity under positive thermal contrast, and a corresponding band 13–14 signal. At the same time, plume-like features associated with nearby oil and gas activity are visible

https://doi.org/10.5194/egusphere-2026-2893
Preprint. Discussion started: 16 June 2026

in the VNIR imagery and radiances, but are not retrieved as NH_3 enhancements. This strengthens the interpretation that the retrieved plume is not driven by generic visible plume structure, but by the NH_3-sensitive TIR band 13–14 signal.

The plume axis does not perfectly coincide with the ERA5 wind direction shown for the scene. This is expected because ERA5 provides grid-scale winds and may not capture local near-source flow, plume-height winds, coastal effects, turbulence, or short-timescale variability at the exact ASTER overpass time. The wind information should therefore be interpreted as a transport constraint for the IME calculation rather than as an exact pixel-scale description of plume motion. Wind uncertainty directly affects the source-rate estimate, in addition to differences in retrieved plume mass and plume-mask geometry.

The retrieval uncertainty and ancillary radiance panels show that not all scene structure is plume-related. This example therefore demonstrates both the strength of the ASTER band 13–14 signal and the need for uncertainty filtering, background correction, source-connected plume masking, and cautious interpretation of wind-driven source-rate variability.

https://doi.org/10.5194/egusphere-2026-2893
Preprint. Discussion started: 16 June 2026

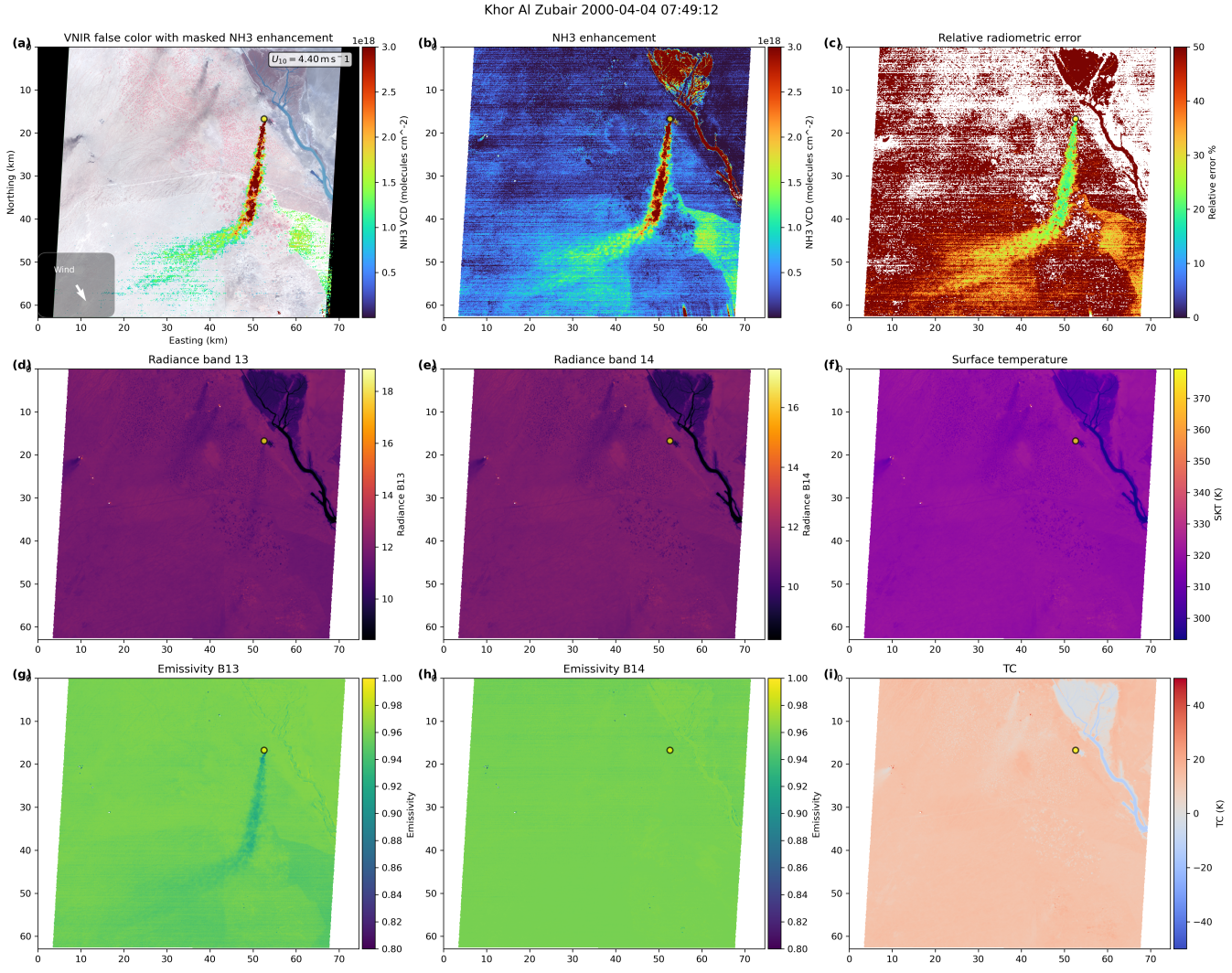

Figure 8. ASTER NH_3 retrieval over Khor Al Zubair on 4 April 2000 (UTC). The panels show VNIR false-color imagery with retrieved NH_3 enhancement overlaid, the unmasked NH_3 enhancement field, relative retrieval uncertainty, observed radiances in TIR bands 13 and 14, ASTER surface temperature, scene-level emissivities in bands 13 and 14, and thermal contrast. The source location is marked in yellow. The scene shows a narrow, source-connected plume under favorable arid conditions with strong thermal contrast. The mismatch between the plume axis and the ERA5 wind direction illustrates the uncertainty of using grid-scale winds for plume-scale flux estimation. Structured retrieval noise is also visible away from the plume, particularly in the lower part of the scene, highlighting that arid backgrounds are not necessarily radiometrically uniform.

All available ASTER scenes over Khor Al Zubair for the period 2000–2025 are processed with the LUT-based retrieval and the IME framework. Each overpass is classified as a successful retrieval, an unusable scene, or a scene with no available data. Unusable scenes include cases affected by cloud cover, weak thermal contrast, insufficient retrieval quality, or other

https://doi.org/10.5194/egusphere-2026-2893
Preprint. Discussion started: 16 June 2026

unfavorable observing conditions. This classification separates successful plume detections from cases where a robust ASTER retrieval could not be obtained.

The resulting time series illustrates the episodic nature of successful ASTER NH_3 retrievals at Khor Al Zubair. Successful plume detections occur only for a subset of available overpasses, while many scenes are rejected by the quality filtering. The figure therefore demonstrates the limited temporal sampling of ASTER plume retrievals rather than a continuous emission record. The source-rate statistics reported here describe the distribution of instantaneous source-rate estimates under favorable observing conditions and should not be interpreted as annual mean emissions.

Retrieved source rates vary substantially between successful overpasses. This spread may reflect real emission variability at the facility, but it can also arise from differences in wind speed, wind direction, wind-field representativeness, plume geometry, plume height, retrieval noise, background subtraction, and plume-mask definition. The successful-scene mean and interquartile range should therefore be interpreted as descriptive statistics of ASTER plume snapshots rather than as a long-term facility-average emission estimate.

As shown in Table 3, the ASTER successful-scene mean of approximately $52\,\mathrm{kt\,yr^{-1}}$ is close to the CrIS-based EMG estimate of $55\,\mathrm{kt\,yr^{-1}}$ from Dammers et al. (2019), but substantially higher than the IASI box-model baseline of $3.9\,\mathrm{kt\,yr^{-1}}$ from Van Damme et al. (2018). The IASI EMG estimates from Dammers et al. (2019) are lower than the CrIS and ASTER values, at approximately 18–19 $\mathrm{kt\,yr^{-1}}$. This spread highlights the importance of retrieval method, spatial resolution, sampling, lifetime assumptions, and wind treatment when comparing satellite-derived NH_3 source rates.

The agreement with the CrIS EMG estimate supports the physical plausibility of the ASTER retrieval for compact plume snapshots, but it should not be interpreted as direct validation. ASTER provides instantaneous high-resolution plume estimates for successful scenes, whereas CrIS and IASI provide multi-year coarse-resolution source estimates with different assumptions about lifetime, plume width, averaging, and wind treatment.

Uncertainties in the Khor Al Zubair source rates are dominated by wind speed, wind direction, the U_{eff} parameterization, plume-mask definition, and retrieval noise. Surface emissivity and co-absorber effects are expected to be smaller than at the other sites because of the arid background, but dust, mineral emissivity variability, and surface temperature structure may still contribute to scene-to-scene variability. The resulting values should therefore be interpreted as effective source rates for the observed plume extent, not as continuous annual emissions.

https://doi.org/10.5194/egusphere-2026-2893
Preprint. Discussion started: 16 June 2026

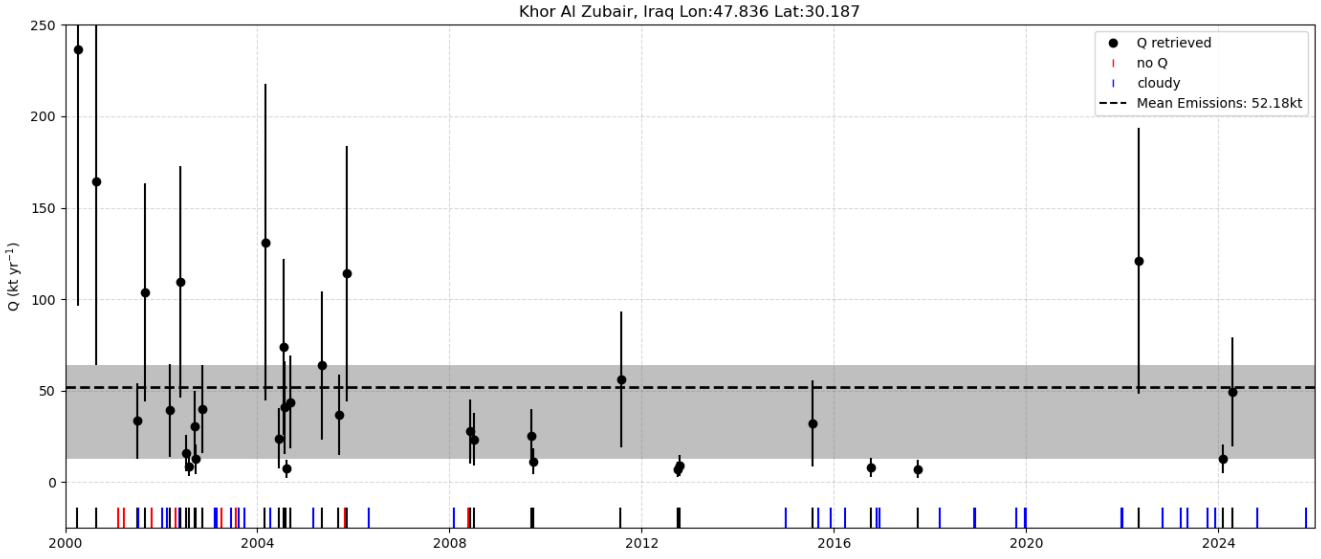

Figure 9. Time series of ASTER-derived NH_3 source rates at Khor Al Zubair for the period 2000–2025. Black points show successful retrievals, with vertical bars indicating retrieval uncertainty. The dashed horizontal line marks the successful-scene mean source rate of approximately 52 kt yr^{-1}, and the gray shaded region denotes the interquartile range. Symbols along the bottom indicate scenes with unsuccessful retrievals due to cloud cover, weak thermal contrast, retrieval-quality filtering, or other unfavorable observing conditions. The value shown is not an annual mean emission, but a mean over successful instantaneous ASTER plume snapshots.

3.2.2 Tolyatti

Tolyatti provides a more challenging test case because the source is located in a temperate and spatially heterogeneous environment. Although the facility is a strong NH_3 emitter, favorable thermal contrast occurs less frequently than at Khor Al Zubair. Surface emissivity variability associated with land cover, infrastructure, and soil moisture also increases the background variability in the retrieved NH_3 field.

Figure 10 shows a favorable ASTER overpass on 14 July 2004. Under these conditions, ASTER detects a coherent NH_3 enhancement extending downwind from the source, with peak enhancements exceeding 10^{18} molecules cm^{-2}. Compared with the Khor Al Zubair scenes, the background shows stronger spatial variability in both the NH_3 enhancement and relative uncertainty fields, consistent with heterogeneous emissivity, land-surface properties and varying thermal contrast. The plume core remains detectable because the NH_3 signal is large enough under the favorable thermal conditions of this overpass.

https://doi.org/10.5194/egusphere-2026-2893
Preprint. Discussion started: 16 June 2026

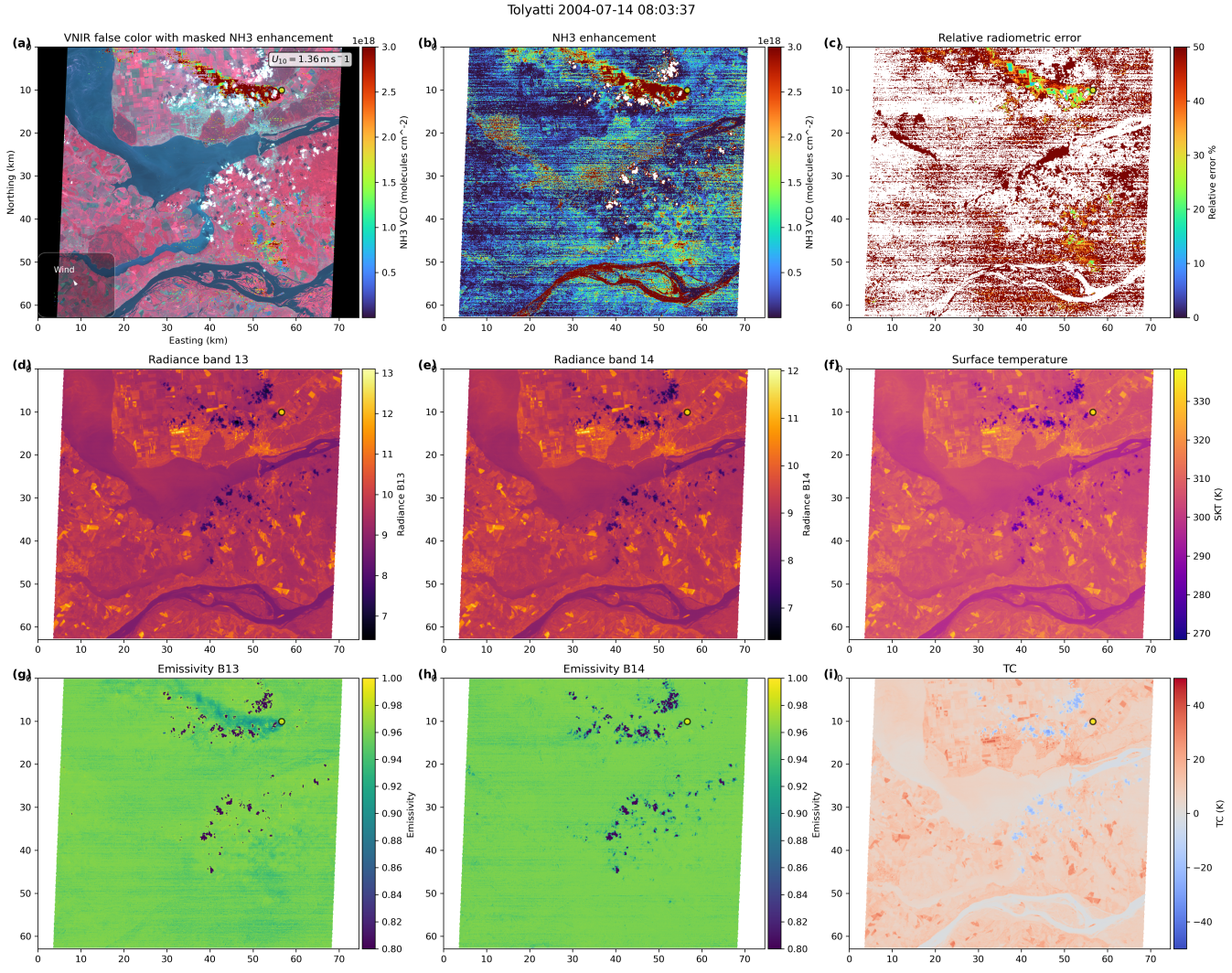

Figure 10. ASTER NH_3 retrieval over Tolyatti on 14 July 2004 (UTC). A coherent plume is visible extending downwind from the source under favorable thermal contrast conditions. Compared with the arid Khor Al Zubair scenes, the background shows increased spatial variability in both the NH_3 enhancement and relative uncertainty fields, consistent with heterogeneous surface emissivity, land cover, and infrastructure.

The time series indicates that successful ASTER retrievals at Tolyatti are limited by observing conditions. Many scenes are rejected because cloud cover, weak thermal contrast, surface heterogeneity, or retrieval-quality filtering prevents robust plume detection. The Tolyatti results therefore show that ASTER can provide high-resolution plume information over non-desert industrial regions, but only episodically. The resulting source-rate statistics should be interpreted as successful-scene instantaneous estimates, not as annual mean emissions.

The literature comparison in Table 3 highlights the importance of method and sampling. The ASTER successful-scene mean of approximately 31 kt yr^{-1} falls between the IASI box-model estimate of 7.4 kt yr^{-1} from Van Damme et al. (2018) and the

https://doi.org/10.5194/egusphere-2026-2893
Preprint. Discussion started: 16 June 2026

larger EMG-based estimates from Dammers et al. (2019), which are 76.6 kt yr^{-1} from CrIS and 66–79 kt yr^{-1} from IASI. This intermediate value should be interpreted cautiously because the ASTER statistic is calculated only from successful plume detections under suitable thermal and surface conditions.

Differences relative to CrIS and IASI may reflect sampling of different emission states, surface heterogeneity, plume masking, wind assumptions, vertical sensitivity, and the different spatial scales of ASTER and hyperspectral sounders. The Tolyatti case therefore demonstrates ASTER detectability in a heterogeneous environment, but does not provide a continuous source-rate record.

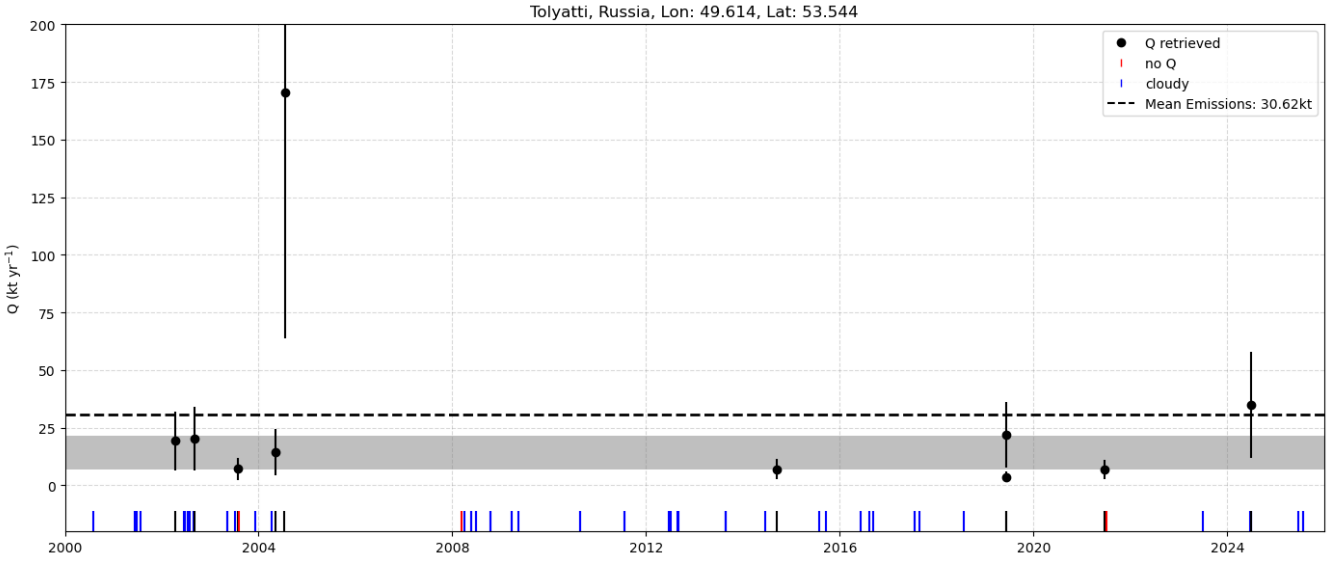

Figure 11. Time series of ASTER-derived NH_3 source rates at Tolyatti for the period 2000–2025. Black points show successful retrievals, with vertical bars indicating retrieval uncertainty. The dashed horizontal line marks the successful-scene mean source rate of approximately 31 kt yr^{-1}, and the gray shaded region denotes the interquartile range. Symbols along the bottom indicate scenes with unsuccessful retrievals due to cloud cover, weak thermal contrast, surface heterogeneity, or retrieval-quality filtering. The value shown is a statistic over successful ASTER plume detections and should not be interpreted as a continuous annual mean emission.

3.2.3 Piesteritz

Piesteritz provides a benchmark for evaluating ASTER NH_3 plume detection close to the lower end of the practical detection range. The site is a well-characterized European fertilizer production facility and has been observed previously with airborne hyperspectral TIR imaging (Noppen et al., 2023). This makes Piesteritz particularly useful for testing whether ASTER can detect moderate industrial NH_3 plumes under favorable but more challenging European surface and thermal conditions.

Figure 12 shows a successful ASTER retrieval over Piesteritz on 28 April 2007. The retrieved enhancement is weaker than for Khor Al Zubair and Tolyatti, but a coherent source-connected structure is visible under suitable observing conditions. The

https://doi.org/10.5194/egusphere-2026-2893
Preprint. Discussion started: 16 June 2026

scene also shows increased background variability and relative uncertainty, illustrating that Piesteritz is close to the practical detection limit of the ASTER method.

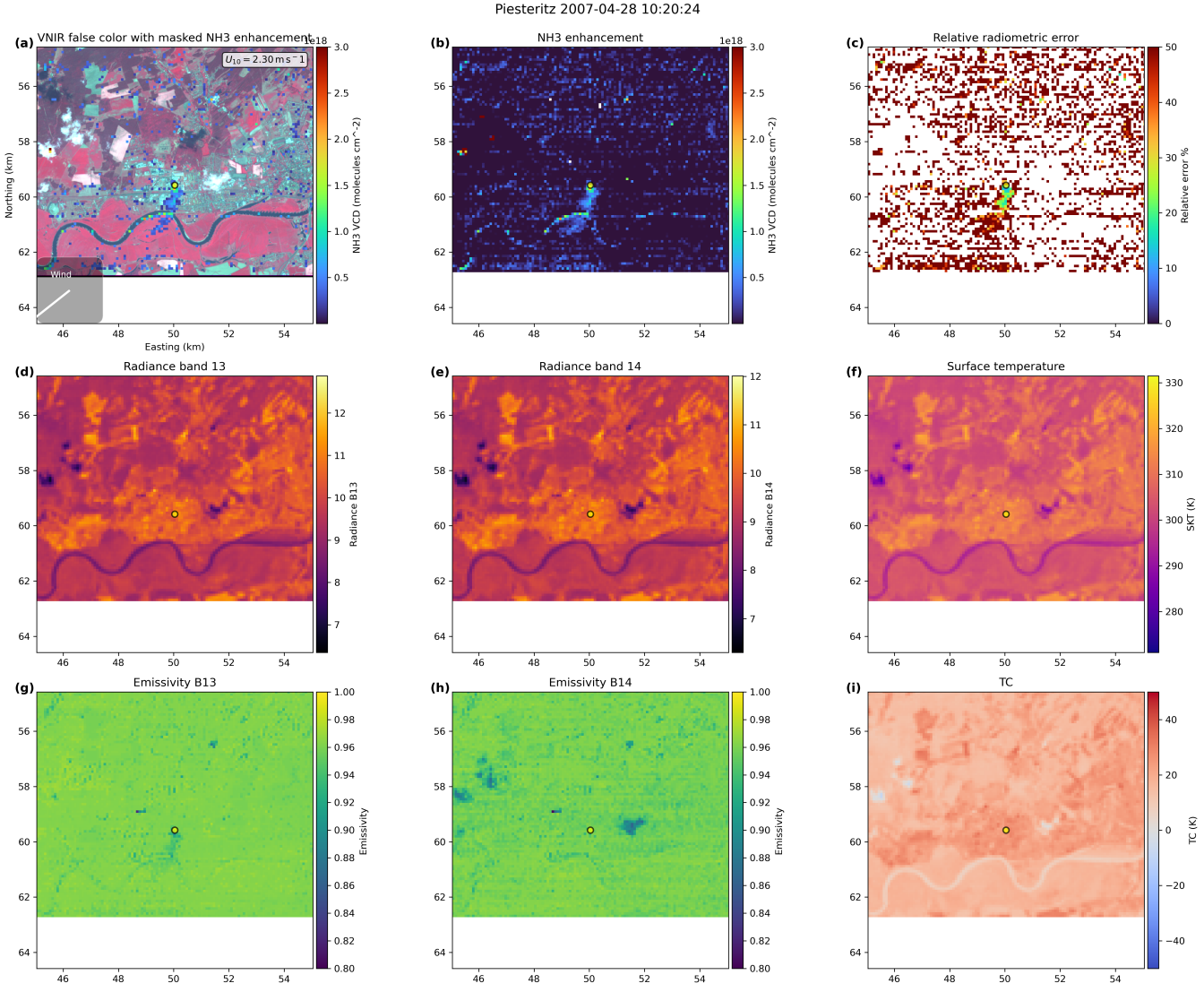

Figure 12. ASTER NH_3 retrieval over Piesteritz on 28 April 2007 (UTC). Panels are as in Fig. 8. The scene illustrates retrieval performance for a smaller European industrial source close to the practical detection limit, where surface heterogeneity, weaker thermal contrast, and retrieval noise strongly affect plume detectability.

The ASTER retrievals over Piesteritz yield a successful-scene mean source rate of approximately 4.0 kt yr^{-1} (Table 3). This value should be interpreted as an instantaneous successful-scene statistic rather than an annual mean emission. Only a small subset of ASTER scenes provides suitable observing conditions, and many retrievals are close to the practical detection limit because of weaker thermal contrast, heterogeneous land cover, and higher background variability than at Khor Al Zubair.

https://doi.org/10.5194/egusphere-2026-2893
Preprint. Discussion started: 16 June 2026

The most relevant independent comparison for Piesteritz is provided by Noppen et al. (2023), who used the airborne Telops Hyper-Cam LW instrument to observe NH_3 plumes over the same facility at 4 m spatial resolution in the longwave infrared. Their detection method was based on a hyperspectral range index, followed by spectral fitting to retrieve NH_3 columns. Fluxes were estimated using both the IME and cross-sectional flux methods, with explicit consideration of two vertical plume scenarios: a non-rising plume and a buoyant plume. Their spring 2021 estimates range from 1.6–3.2 kt yr^{-1} with IME and 2.2–5.4 kt yr^{-1} with CSF (Table 3). These values are consistent in magnitude with the ASTER successful-scene mean of approximately 4.0 kt yr^{-1}.

This agreement is encouraging because the two approaches differ substantially in spatial resolution, spectral information, retrieval method, and temporal sampling. Hyper-Cam LW provides hyperspectral measurements at meter-scale resolution and can explicitly fit interfering species and surface temperature, whereas ASTER relies on broadband multispectral radiances and a LUT-based split-window observable. In addition, Noppen et al. (2023) showed that plume altitude and thermal contrast can strongly affect retrieved NH_3 columns. These same factors are expected to influence the ASTER retrieval, especially because the ASTER method assumes a simplified near-surface NH_3 vertical distribution. The consistency with the airborne range therefore supports the physical plausibility of the ASTER Piesteritz retrievals, but does not constitute direct validation of individual ASTER overpasses.

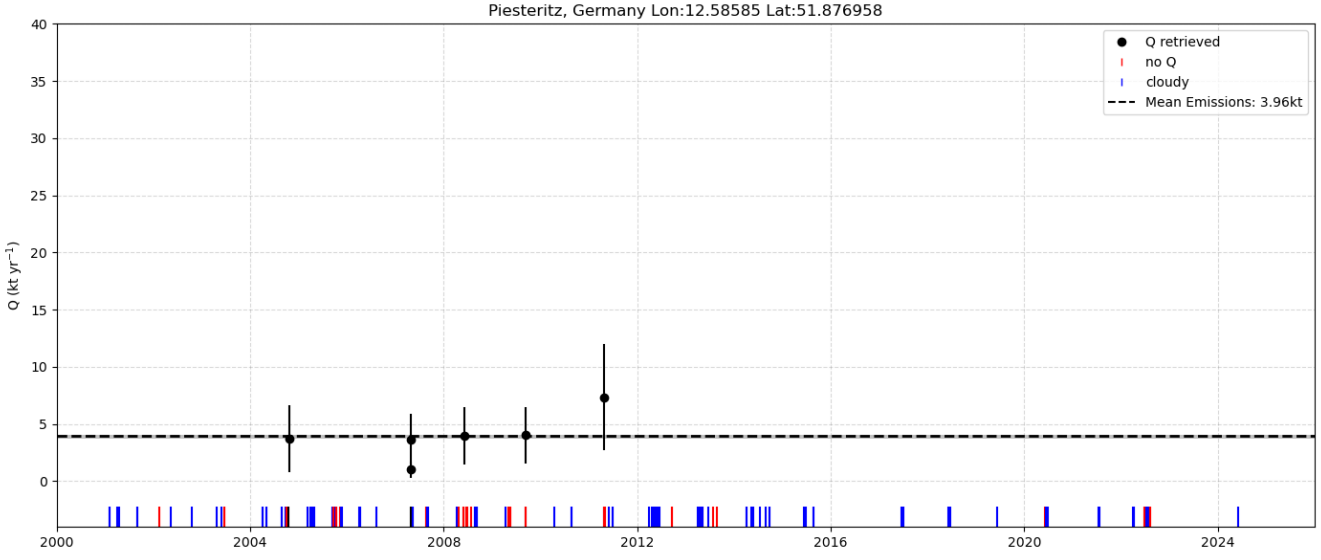

Figure 13. Time series of ASTER-derived NH_3 source rates at Piesteritz for the period 2000–2025. Black points show successful retrievals, with vertical bars indicating retrieval uncertainty. The dashed horizontal line marks the successful-scene mean source rate of approximately 4.0 kt yr^{-1}, and the gray shaded region denotes the interquartile range. Symbols along the bottom indicate scenes with unsuccessful retrievals due to cloud cover, weak thermal contrast, surface heterogeneity, or retrieval-quality filtering. The ASTER value is not an annual mean emission, but a mean over successful instantaneous ASTER plume snapshots.

https://doi.org/10.5194/egusphere-2026-2893
Preprint. Discussion started: 16 June 2026

4 Discussion

This study demonstrates that multispectral TIR imaging can detect NH_3 plumes at facility scale under favorable observing conditions. Although ASTER has only five broad TIR bands, band 13 overlaps with the NH_3 ν_2 absorption region and retains measurable sensitivity after convolution with the instrument SRFs. The differential response between bands 13 and 14 provides a physically interpretable observable for plume detection at 90 m spatial resolution. This spatial resolution enables plume-scale source attribution that is not possible with current hyperspectral sounders such as IASI and CrIS.

The sensitivity analysis shows that thermal contrast is the primary control on ASTER NH_3 detectability. When the surface is warmer than the NH_3-bearing layer, NH_3 absorbs radiation from the warmer surface background and reduces the top-of-atmosphere radiance measured in band 13. Around zero thermal contrast, the radiance response to NH_3 becomes weak and the retrieval becomes noise dominated. For stronger thermal contrast, the LUT sensitivity increases and the noise-equivalent NH_3 column decreases to values of order 10^{17}–10^{18} molecules cm^{-2} under favorable conditions. These values should be interpreted as theoretical single-pixel sensitivity limits, not as guaranteed plume detection thresholds.

In real ASTER scenes, practical plume detection is more restrictive than the idealized noise-equivalent limit. Robust detections require spatially coherent enhancements, favorable thermal contrast, sufficient radiometric precision, and limited surface-related structure in the band ratio. This explains why the method performs best over Khor Al Zubair, where hot arid conditions often provide strong thermal contrast and limited cloud contamination. However, the desert background is not automatically low-noise. Mineral emissivity variability, surface temperature structure, suspended dust, and dust storms can affect the TIR radiances and may contribute to structured retrieval noise in parts of the scene (Ginoux et al., 2012; Someya et al., 2020). Tolyatti and Piesteritz show that ASTER can also detect NH_3 plumes in more heterogeneous environments, but with reduced sampling and larger sensitivity to surface emissivity variability, retrieval noise, and plume-mask definition.

The comparison with published source-rate estimates provides useful context but should not be interpreted as direct validation. For Khor Al Zubair, the ASTER successful-scene mean is close to the CrIS EMG estimate from Dammers et al. (2019), but higher than the IASI box-model baseline from Van Damme et al. (2018). For Tolyatti, the ASTER estimate lies between the lower IASI box-model estimate from Van Damme et al. (2018) and the larger CrIS and IASI EMG estimates from Dammers et al. (2019). For Piesteritz, the ASTER successful-scene mean is consistent in magnitude with the airborne Hyper-Cam LW estimates from Noppen et al. (2023). The spread between studies is large and strongly method dependent, reflecting differences in spatial resolution, temporal sampling, plume treatment, lifetime assumptions, wind treatment, and vertical sensitivity.

The Piesteritz comparison is particularly informative because Noppen et al. (2023) used high-resolution airborne hyperspectral TIR imaging and explicitly tested the effect of plume-rise assumptions on retrieved NH_3 columns and fluxes. Their results show that thermal contrast and vertical plume distribution can strongly affect flux estimates, and that the sensitivity to plume-height assumptions decreases when thermal contrast is more favorable. This supports one of the main limitations identified for ASTER: plume detection can be robust under favorable conditions, while quantitative source-rate estimates remain sensitive to the assumed vertical distribution of NH_3. Future work could reduce this uncertainty by coupling the retrieval to plume trans-

https://doi.org/10.5194/egusphere-2026-2893
Preprint. Discussion started: 16 June 2026

port modelling, for example using HYSPLIT or a similar Lagrangian dispersion model to test plausible plume heights, vertical distributions, and transport pathways for each overpass (Stein et al., 2015).

Flux estimation is therefore more uncertain than plume detection. The IME method depends on the retrieved plume mass, plume mask, background subtraction, wind speed, wind direction, plume length scale, and the effective wind speed parameterization. In this study, wind information is taken from ERA5 and used as a grid-scale transport constraint. This provides a practical first-order estimate, but it may not represent plume-scale winds at the emission height or at the exact ASTER overpass time. Local flow, coastal effects, boundary-layer structure, plume rise, turbulence, and short-timescale wind variability can all contribute to differences between the observed plume direction and the ERA5 wind direction. Because the IME source rate scales with the effective wind speed, wind-field uncertainty directly affects the retrieved Q, in addition to differences in retrieved plume mass and plume-mask geometry. The U_{eff} parameterization used here was originally developed for methane plumes and is not necessarily optimal for NH_3, where deposition, chemistry, plume rise, and near-source vertical mixing may influence the observed plume mass. The source rates reported here should therefore be interpreted as instantaneous effective source-rate estimates for the observed plume extent, not as annual mean emissions or continuous facility-average emissions.

Surface emissivity remains a major systematic uncertainty. In this study, emissivity is prescribed using ASTER GED V3 rather than retrieved independently for each plume scene. This avoids absorbing plume-induced band 13 radiance reductions into scene-specific emissivity retrievals, but it cannot fully represent day-to-day or sub-pixel variations in land surface properties. This limitation is relevant not only for heterogeneous vegetated and urban scenes, such as Tolyatti and Piesteritz, but also for arid scenes where mineral emissivity variability, surface temperature structure, suspended dust, and dust storms can affect the TIR radiances. Future retrievals should quantify the sensitivity to emissivity assumptions by perturbing the prescribed emissivity, for example by 0.005–0.01, and by testing band-dependent emissivity constraints.

The current LUT treats NH_3 as the only variable absorber. This is suitable for demonstrating feasibility, but it can introduce biases in industrial regions where other gases, aerosols, dust, smoke, or surface features affect the same broad ASTER bands. Several diagnostics support the interpretation of the retrieved structures as NH_3 plumes: the enhancements are strongest in the NH_3-sensitive band 13 relative to band 14, are spatially connected to known industrial NH_3 sources, show coherent plume-like morphology, and occur under thermal-contrast conditions where the LUT predicts measurable NH_3 sensitivity. Repeated detections at Khor Al Zubair further support the robustness of the signal. However, these diagnostics cannot fully eliminate interference from other absorbers or surface effects.

ASTER is not an operational NH_3 monitoring instrument. Its revisit frequency, cloud sensitivity, and dependence on thermal contrast limit temporal sampling. The method is therefore best suited for retrospective analysis of favorable scenes over large, persistent sources, and for plume-scale source attribution rather than routine emissions monitoring. Nevertheless, the long ASTER archive provides a valuable opportunity to identify historical plume events and to complement coarse-resolution hyperspectral sounders.

The retrieval framework is transferable to other multispectral TIR imagers with suitable spectral coverage. Instruments such as the ECOsystem Spaceborne Thermal Radiometer Experiment on Space Station (ECOSTRESS) and the Landsat Thermal Infrared Sensor (TIRS) provide complementary high-resolution TIR observations with different spatial, spectral, and sampling

https://doi.org/10.5194/egusphere-2026-2893
Preprint. Discussion started: 16 June 2026

characteristics (Reuter et al., 2015; Fisher et al., 2020). Future missions with improved spatial, spectral, and temporal coverage could enable more systematic NH_3 plume monitoring. A more targeted TIR imaging concept, with bands placed around the NH_3 ν_2 absorption feature and nearby reference windows, could improve point-source sensitivity relative to a broad-band instrument such as ASTER. This could support a future observing strategy in which wide-area NH_3 mappers are complemented by high-spatial-resolution point-source imagers, analogous to the emerging split in CH_4 remote sensing. More broadly, these results show that high-resolution TIR band imagers can complement hyperspectral sounders by resolving plume structure around individual sources.

5 Conclusions

We developed and tested a physically based retrieval framework for detecting NH_3 plumes from ASTER multispectral TIR observations. The method combines TFIT radiative transfer simulations, a LUT-based inversion, scene-level radiance correction, plume segmentation, and IME-based source-rate estimation. NH_3 enhancements are retrieved from the differential response of ASTER bands 13 and 14, with band 13 providing sensitivity to NH_3 absorption and band 14 acting as a nearby reference channel.

Sensitivity simulations show that ASTER can preserve measurable NH_3 radiance signals after convolution with the broad TIR spectral response functions. Detectability depends strongly on thermal contrast. Around zero thermal contrast, the NH_3 signal becomes weak and retrievals are noise dominated. For stronger thermal contrast, sensitivity improves and theoretical single-pixel noise-equivalent columns reach values of order 10^{17}–10^{18} molecules cm^{-2} under favorable conditions.

Application to industrial point sources demonstrates that ASTER can resolve NH_3 plume structure at 90 m spatial resolution. Khor Al Zubair provides the clearest demonstration, with repeated successful detections under favorable desert conditions. Tolyatti shows that ASTER can detect plumes in a more heterogeneous non-desert environment, but only episodically. Piesteritz demonstrates that moderate European industrial sources can be detected under suitable conditions, close to the practical sensitivity limit of the method.

The strongest result of this study is plume detection and source attribution. Source-rate estimates derived with the IME method are useful as instantaneous effective estimates for successful plume scenes, but they remain sensitive to wind speed, wind direction, wind-field representativeness, plume masking, background subtraction, vertical plume distribution, emissivity assumptions, and possible spectral interference. The successful-scene means reported here should therefore not be interpreted as annual mean emissions.

Comparison with published IASI, CrIS, and airborne Hyper-Cam LW estimates shows that the ASTER source-rate statistics are generally within the broad range of previous satellite and airborne estimates, but the spread is large and method dependent. This reinforces that ASTER provides complementary plume-scale information rather than a direct replacement for hyperspectral satellite or airborne retrievals.

These results establish that high-resolution multispectral TIR imagers can complement hyperspectral NH_3 sounders by resolving facility-scale plume structure. While ASTER cannot provide routine monitoring for most NH_3 sources, its archive

https://doi.org/10.5194/egusphere-2026-2893
Preprint. Discussion started: 16 June 2026

enables retrospective analysis of favorable scenes over large emitters. Future work should focus on emissivity sensitivity tests, multi-species LUTs, NH_3-specific transport parameterizations, improved characterization of plume-scale winds, improved radiance-correction characterization, and application to additional current and future TIR imaging instruments.

Code availability. The TFIT radiative transfer code used in this study is not publicly archived, but is available from the corresponding author upon reasonable request. TFIT uses spectroscopic parameters from the HITRAN database accessed through the HITRAN Application Programming Interface (HAPI) (Kochanov et al., 2016).

Data availability. ASTER Level 1B radiance (AST_L1B, Version 4), surface emissivity (AST_05, Version 4) surface kinetic temperature (AST_08, Version 4) and Global Emissivity Database Version 3 (ASTER GED V3) products are publicly available from the NASA Land Processes Distributed Active Archive Center (LP DAAC) through the Earthdata platform (https://earthdata.nasa.gov/). The data can be accessed using spatial and temporal queries through the LP DAAC data portal or programmatically via the Earthaccess Python interface (https://github.com/nsidc/earthaccess). Meteorological fields used for scene characterization and wind information are obtained from ECMWF reanalysis products.

Author contributions. LBT implemented and applied the retrieval framework, performed the formal data analysis, and prepared the manuscript. LBT, TW, and ED contributed to the conceptual design of the study. LBT, TW, and ED jointly developed the TFIT radiative transfer model and retrieval methods. ED contributed to satellite context and interpretation of source-rate estimates. ED and TW contributed to the interpretation of the results. All authors reviewed the final manuscript.

Competing interests. The authors declare that they have no conflict of interest.

Acknowledgements. The authors acknowledge the NASA Land Processes Distributed Active Archive Center for providing the ASTER data products used in this study. The authors also acknowledge ECMWF for meteorological reanalysis data used in the retrieval workflow. Generative AI tools were used to assist with language refinement and editorial clarity; all scientific analysis, interpretation, and conclusions are the authors' own work.

https://doi.org/10.5194/egusphere-2026-2893
Preprint. Discussion started: 16 June 2026

References

Abrams, M., Tsu, H., Hulley, G., Iwao, K., Pieri, D., Cudahy, T., and Kargel, J.: The advanced spaceborne thermal emission and reflection radiometer (ASTER) after fifteen years: review of global products, International Journal of Applied Earth Observation and Geoinformation, 38, 292–301, 2015.

Arai, K. and Tonooka, H.: Radiometric performance evaluation of ASTER VNIR, SWIR, and TIR, IEEE Transactions on Geoscience and Remote Sensing, 43, 2725–2732, 2005.

Bobbink, R., Hornung, M., and Roelofs, J. G. M.: The effects of air-borne nitrogen pollutants on species diversity in natural and semi-natural European vegetation, Journal of ecology, 86, 717–738, 1998.

Brunekreef, B. and Holgate, S. T.: Air pollution and health, The lancet, 360, 1233–1242, 2002.

Campion, R., Salerno, G. G., Coheur, P.-F., Hurtmans, D., Clarisse, L., Kazahaya, K., Burton, M., Caltabiano, T., Clerbaux, C., and Bernard, A.: Measuring volcanic degassing of SO2 in the lower troposphere with ASTER band ratios, Journal of Volcanology and Geothermal Research, 194, 42–54, 2010.

Clarisse, L., Clerbaux, C., Franco, B., Hadji-Lazaro, J., Whitburn, S., Kopp, A., Hurtmans, D., and Coheur, P.-F.: A decadal data set of global atmospheric dust retrieved from IASI satellite measurements, Journal of Geophysical Research: Atmospheres, 124, 1618–1647, 2019.

Clarisse, L., Franco, B., Van Damme, M., Di Gioacchino, T., Hadji-Lazaro, J., Whitburn, S., Noppen, L., Hurtmans, D., Clerbaux, C., and Coheur, P.: The IASI NH 3 version 4 product: averaging kernels and improved consistency, Atmospheric Measurement Techniques Discussions, 2023, 1–31, 2023.

Cusworth, D. H., Thorpe, A. K., Ayasse, A. K., Stepp, D., Heckler, J., Asner, G. P., Miller, C. E., Yadav, V., Chapman, J. W., and Eastwood, M. L.: Strong methane point sources contribute a disproportionate fraction of total emissions across multiple basins in the United States, Proceedings of the National Academy of Sciences, 119, e2202338 119, 2022.

Dammers, E., McLinden, C. A., Griffin, D., Shephard, M. W., Van Der Graaf, S., Lutsch, E., Schaap, M., Gainairu-Matz, Y., Fioletov, V., and Van Damme, M.: NH3 emissions from large point sources derived from CrIS and IASI satellite observations, Atmospheric Chemistry and Physics, 19, 12 261–12 293, 2019.

De Vries, W., Hettelingh, J.-P., and Posch, M.: Critical loads and dynamic risk assessments: Nitrogen, acidity and metals in terrestrial and aquatic ecosystems, vol. 25, Springer, 2015.

Erisman, J. W., Sutton, M. A., Galloway, J., Klimont, Z., and Winiwarter, W.: How a century of ammonia synthesis changed the world, Nature geoscience, 1, 636–639, 2008.

European Environment Agency: Industrial reporting under the Industrial Emissions Directive 2010/75/EU and European Pollutant Release and Transfer Register Regulation (EC) No 166/2006, 2021.

Fisher, J. B., Lee, B., Purdy, A. J., Halverson, G. H., Dohlen, M. B., Cawse-Nicholson, K., Wang, A., Anderson, R. G., Aragon, B., Arain, M. A., et al.: ECOSTRESS: NASA's next generation mission to measure evapotranspiration from the international space station, Water Resources Research, 56, e2019WR026 058, 2020.

Fowler, D., Pilegaard, K., Sutton, M. A., Ambus, P., Raivonen, M., Duyzer, J., Simpson, D., Fagerli, H., Fuzzi, S., and Schjoerring, J. K.: Atmospheric composition change: ecosystems–atmosphere interactions, Atmospheric Environment, 43, 5193–5267, 2009.

Frankenberg, C., Thorpe, A. K., Thompson, D. R., Hulley, G., Kort, E. A., Vance, N., Borchardt, J., Krings, T., Gerilowski, K., Sweeney, C., et al.: Airborne methane remote measurements reveal heavy-tail flux distribution in Four Corners region, Proceedings of the national academy of sciences, 113, 9734–9739, 2016.

https://doi.org/10.5194/egusphere-2026-2893
Preprint. Discussion started: 16 June 2026

Galloway, J. N., Aber, J. D., Erisman, J. W., Seitzinger, S. P., Howarth, R. W., Cowling, E. B., and Cosby, B. J.: The nitrogen cascade, Bioscience, 53, 341–356, 2003.

Gillespie, A. R., Abbott, E. A., Gilson, L., Hulley, G., Jiménez-Muñoz, J.-C., and Sobrino, J. A.: Residual errors in ASTER temperature and emissivity standard products AST08 and AST05, Remote sensing of environment, 115, 3681–3694, 2011.

Ginoux, P., Prospero, J. M., Gill, T. E., Hsu, N. C., and Zhao, M.: Global-scale attribution of anthropogenic and natural dust sources and their emission rates based on MODIS Deep Blue aerosol products, Reviews of Geophysics, 50, 2012.

Gorroño, J., Varon, D. J., Irakulis-Loitxate, I., and Guanter, L.: Understanding the potential of Sentinel-2 for monitoring methane point emissions, Atmospheric Measurement Techniques, 16, 89–107, 2023.

Goudar, M., Anema, J. C., Kumar, R., Borsdorff, T., and Landgraf, J.: Plume detection and emission estimate for biomass burning plumes from TROPOMI carbon monoxide observations using APE v1. 1, Geoscientific Model Development, 16, 4835–4852, 2023.

Han, Y., Revercomb, H., Cromp, M., Gu, D., Johnson, D., Mooney, D., Scott, D., Strow, L., Bingham, G., Borg, L., et al.: Suomi NPP CrIS measurements, sensor data record algorithm, calibration and validation activities, and record data quality, Journal of Geophysical Research: Atmospheres, 118, 12–734, 2013.

Hilton, F., Armante, R., August, T., Barnet, C., Bouchard, A., Camy-Peyret, C., Capelle, V., Clarisse, L., Clerbaux, C., Coheur, P.-F., et al.: Hyperspectral Earth observation from IASI: Five years of accomplishments, bulletin of the american meteorological Society, 93, 347–370, 2012.

Janssens-Maenhout, G., Crippa, M., Guizzardi, D., Dentener, F., Muntean, M., Pouliot, G., Keating, T., Zhang, Q., Kurokawa, J., Wankmüller, R., et al.: HTAP_v2. 2: a mosaic of regional and global emission grid maps for 2008 and 2010 to study hemispheric transport of air pollution, Atmospheric Chemistry and Physics, 15, 11 411–11 432, 2015.

Kochanov, R., Gordon, I., Rothman, L., Wcisło, P., Hill, C., and Wilzewski, J.: HITRAN Application Programming Interface (HAPI): A comprehensive approach to working with spectroscopic data, Journal of Quantitative Spectroscopy and Radiative Transfer, 177, 15–30, https://doi.org/https://doi.org/10.1016/j.jqsrt.2016.03.005, xVIIIth Symposium on High Resolution Molecular Spectroscopy (HighRus-2015), Tomsk, Russia, 2016.

Kuai, L., Kalashnikova, O. V., Hopkins, F. M., Hulley, G. C., Lee, H., Garay, M. J., Duren, R. M., Worden, J. R., and Hook, S. J.: Quantification of ammonia emissions with high spatial resolution thermal infrared observations from the hyperspectral thermal emission spectrometer (HyTES) airborne instrument, IEEE Journal of Selected Topics in Applied Earth Observations and Remote Sensing, 12, 4798–4812, 2019.

Kuenen, J., Dellaert, S., Visschedijk, A., Jalkanen, J.-P., Super, I., and Denier van der Gon, H.: CAMS-REG-v4: a state-of-the-art high-resolution European emission inventory for air quality modelling, Earth System Science Data, 14, 491–515, 2022.

NASA JPL: ASTER Global Emissivity Dataset, 100-meter, HDF5, https://doi.org/10.5067/COMMUNITY/ASTER_GED/AG100.003, accessed: 15 May 2026, 2014.

NASA/METI/AIST/Japan Spacesystems and U.S./Japan ASTER Science Team: ASTER L2 Surface Emissivity V004, https://doi.org/10.5067/ASTER/AST_05.004, accessed: 15 May 2026, 2025a.

NASA/METI/AIST/Japan Spacesystems and U.S./Japan ASTER Science Team: ASTER L2 Surface Kinetic Temperature V004, https://doi.org/10.5067/ASTER/AST_08.004, accessed: 15 May 2026, 2025b.

NASA/METI/AIST/Japan Spacesystems and U.S./Japan ASTER Science Team: ASTER L1B Registered Radiance at the Sensor V004, https://doi.org/10.5067/ASTER/AST_L1B.004, accessed: 15 May 2026, 2025c.

Noppen, L., Clarisse, L., Tack, F., Ruhtz, T., Merlaud, A., Van Damme, M., Van Roozendael, M., Schuettemeyer, D., and Coheur, P.: Constraining industrial ammonia emissions using hyperspectral infrared imaging, Remote Sensing of Environment, 291, 113 559, 2023.

https://doi.org/10.5194/egusphere-2026-2893
Preprint. Discussion started: 16 June 2026

Noppen, L., Clarisse, L., Tack, F., Ruhtz, T., Van Damme, M., Van Roozendael, M., Schuettemeyer, D., and Coheur, P.: Towards a low-resolution infrared sounder for monitoring atmospheric ammonia (NH 3) at high spatial resolution, EGUsphere, 2025, 1–29, 2025.

Reuter, D. C., Richardson, C. M., Pellerano, F. A., Irons, J. R., Allen, R. G., Anderson, M., Jhabvala, M. D., Lunsford, A. W., Montanaro, M., Smith, R. L., et al.: The Thermal Infrared Sensor (TIRS) on Landsat 8: Design overview and pre-launch characterization, Remote Sensing, 7, 1135–1153, 2015.

Shephard, M. W., Dammers, E., Cady-Pereira, K. E., Kharol, S. K., Thompson, J., Gainariu-Matz, Y., Zhang, J., McLinden, C. A., Kovachik, A., Moran, M., et al.: Ammonia measurements from space with the Cross-track Infrared Sounder: characteristics and applications, Atmospheric Chemistry and Physics, 20, 2277–2302, 2020.

Skjøth, C. A. and Geels, C.: The effect of climate and climate change on ammonia emissions in Europe, Atmospheric Chemistry and Physics, 13, 117–128, 2013.

Someya, Y., Imasu, R., Shiomi, K., and Saitoh, N.: Atmospheric ammonia retrieval from the TANSO-FTS/GOSAT thermal infrared sounder, Atmospheric Measurement Techniques, 13, 309–321, 2020.

Stein, A. F., Draxler, R. R., Rolph, G. D., Stunder, B. J., Cohen, M. D., and Ngan, F.: NOAA's HYSPLIT atmospheric transport and dispersion modeling system, Bulletin of the American Meteorological Society, 96, 2059–2077, 2015.

Van Damme, M., Clarisse, L., Heald, C. L., Hurtmans, D., Ngadi, Y., Clerbaux, C., Dolman, A. J., Erisman, J. W., and Coheur, P.-F.: Global distributions, time series and error characterization of atmospheric ammonia (NH 3) from IASI satellite observations, Atmospheric chemistry and physics, 14, 2905–2922, 2014.

Van Damme, M., Clarisse, L., Whitburn, S., Hadji-Lazaro, J., Hurtmans, D., Clerbaux, C., and Coheur, P.-F.: Industrial and agricultural ammonia point sources exposed, Nature, 564, 99–103, 2018.

Varon, D. J., Jacob, D. J., McKeever, J., Jervis, D., Durak, B. O. A., Xia, Y., and Huang, Y.: Quantifying methane point sources from fine-scale satellite observations of atmospheric methane plumes, Atmospheric Measurement Techniques, 11, 5673–5686, 2018.

Varon, D. J., McKeever, J., Jervis, D., Maasakkers, J. D., Pandey, S., Houweling, S., Aben, I., Scarpelli, T., and Jacob, D. J.: Satellite discovery of anomalously large methane point sources from oil/gas production, Geophysical Research Letters, 46, 13 507–13 516, 2019.

Varon, D. J., Jervis, D., Pandey, S., Gallardo, S. L., Balasus, N., Yang, L. H., and Jacob, D. J.: Quantifying NOx point sources with Landsat and Sentinel-2 satellite observations of NO2 plumes, Proceedings of the National Academy of Sciences, 121, e2317077 121, 2024.

Yamaguchi, Y., Kahle, A. B., Tsu, H., Kawakami, T., and Pniel, M.: Overview of Advanced Spaceborne Thermal Emission and Reflection Radiometer (ASTER), IEEE Transactions on Geoscience and Remote Sensing, 36, 1062–1071, 1998.